HHS Public Access

Author manuscript

Immunity. Author manuscript; available in PMC 2020 August 20.

Published in final edited form as:

Immunity. 2019 August 20; 51(2): 241–257.e9. doi:10.1016/j.immuni.2019.06.005.

The cytokine TNF promotes transcription factor SREBP activity and binding to inflammatory genes to activate macrophages and limit tissue repair

Anthony Kusnadi[1,3,6], **Sung Ho Park**[3,5,6], **Ruoxi Yuan**[3], **Tania Pannellini**[3], **Eugenia Giannopoulou**[3,4], **David Oliver**[3], **Theresa Lu**[1,3], **Kyung-Hyun Park-Min**[2,3,*], **Lionel B. Ivashkiv**[1,3,7,*]

[1]Immunology and Microbial Pathogenesis Program, Weill Cornell Graduate School of Medical Sciences, New York, NY 10021, USA

[2]BCMB Allied Program, Weill Cornell Graduate School of Medical Sciences, New York, NY 10021, USA

[3]Research Institute and the David Z. Rosensweig Genomics Research Center, Hospital for Special Surgery, New York, NY 10021, USA

[4]Biological Sciences Department, New York City College of Technology, City University of New York, Brooklyn, NY 11201, USA

[5]School of Life Sciences, Ulsan National Institute of Science & Technology (UNIST), Ulsan, 44919 Korea

[6]These authors contributed equally

[7]Lead Contact

SUMMARY

Cytokine TNF-mediated macrophage polarization is important for inflammatory disease pathogenesis, but the mechanisms regulating polarization are not clear. We performed transcriptomic and epigenomic analysis of the TNF response in primary human macrophages and reveal late phase activation of SREBP2, the master regulator of cholesterol biosynthesis genes. TNF stimulation extended the genomic profile of SREBP2 occupancy to include binding to and

*Correspondence: parkmink@hss.edu (K.–H. P.–M.), ivashkivl@hss.edu (L.B.I.).

AUTHOR CONTRIBUTIONS

A.K. conceptualized, designed, and performed most of the experiments. S.H.P. performed the majority of the bioinformatic analysis and generated some of the RNAseq, ChIP-seq (for histone marks), and ATAC-seq data sets. R.Y. assisted with some of the wound healing experiments. T.P. provided analysis of the the histopathology. D.O. and E.G. performed bioinformatic analysis. T.L. contributed her expertise. K.-H. P.-M. and L.B.I. conceptualized and oversaw the study and edited the manuscript. All authors reviewed and provided input on the manuscript.

DECLARATION OF INTERESTS

L.B.I. consults for Lilly but does not accept any personal compensation. The other authors declare no competing interests. (Butler et al., 2018; Chia et al., 2016; Dobin et al., 2013; Folch et al., 1957; Heinz et al., 2010; Langmead and Salzberg, 2012; McLean et al., 2010; Robinson et al., 2010; Toth et al., 2004; Trapnell et al., 2013)

activation of inflammatory and interferon response genes independently of its functions in sterol metabolism. Genetic ablation of SREBP function shifted the balance of macrophage polarization from an inflammatory to a reparative phenotype in peritonitis and skin wound healing models. Genetic ablation of SREBP activity in myeloid cells or topical pharmacological inhibition of SREBP improved skin wound healing under homeostatic and chronic inflammatory conditions. Our results identify a function and mechanism of action for SREBPs in augmenting TNF-induced macrophage activation and inflammation, and open therapeutic avenues for promoting wound repair.

Graphical Abstract

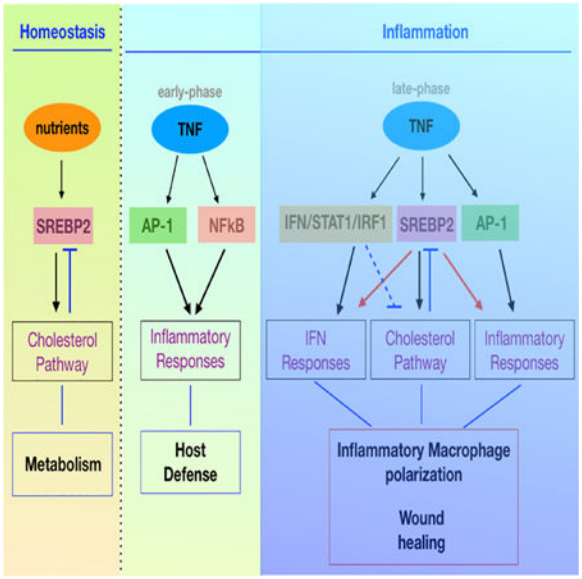

TNF-mediated macrophage polarization is important for inflammatory disease pathogenesis, but the mechanisms regulating polarization are not clear. Kusnadi et al. find that TNF stimulation of macrophages results in late phase activation of cholesterol regulator SREBP2. SREBP2 binds to inflammatory and interferon response target genes and promotes inflammation. Inhibition of SREBP activity promotes M2-like polarization and improves wound healing.

INTRODUCTION

TNF plays critical roles in inflammation, host defense against pathogens, and the pathogenesis of chronic inflammatory diseases (Brenner et al., 2015; Kalliolias and Ivashkiv, 2016; Medzhitov, 2008; Nathan and Ding, 2010). TNF signaling rapidly but transiently activates canonical NF-κB target genes such as *IL1B*, *IL6* and *IL8* (Brenner et al., 2015; Kalliolias and Ivashkiv, 2016). Less is known about the subsequent late phase of the cellular TNF response, although TNF is generally considered to polarize macrophages towards a classical inflammatory (also termed M1-like) state (Lawrence and Natoli, 2011) (Huynh et al., 2016; Kalliolias and Ivashkiv, 2016; Park et al., 2017; Yarilina et al., 2008).

Sterol Response Element Binding Factors (SREBFs, and also known as SREBPs) are the master transcription factors that regulate cellular lipid metabolism (Brown and Goldstein, 1997; Goldstein and Brown, 2015). SREBP1 preferentially promotes fatty acid synthesis, while SREBP2 regulates cellular cholesterol levels by directly activating genes that encode the majority of enzymes in the cholesterol biosynthesis pathway (Horton et al., 2002). SREBPs are constitutively expressed, bind to their chaperone SCAP (SREBP Cleavage-activating Protein), and under cholesterol-replete conditions are retained in the ER membrane by the negative regulators INSIG1 and INSIG2. When the cellular sterol supply is depleted, the SCAP-SREBP complex dissociates from INSIGs and translocates to the Golgi where SREBPs undergo proteolytic cleavage that releases an amino-terminal fragment (N-SREBP) that translocates to the nucleus and is transcriptionally active (Brown and Goldstein, 1997). N-SREBP2 binds to sterol regulatory elements (SREs) to activate its canonical target genes in cooperation with other transcription factors, including SP1, NF-Y, and CREB/ATF (Osborne and Espenshade, 2009).

An important role for SREBP in immune responses is increasingly appreciated. During immune cell activation, SREBPs, acting via cholesterol-pathway sterol metabolites, have been implicated in T cell proliferation, NK cell effector function, antiviral responses, activation of the AIM2 and NLRP1 inflammasomes, and priming of trained immunity by b-glucan (Assmann et al., 2017; Bekkering et al., 2018; Dang et al., 2017; DeBose-Boyd and Ye, 2018; Fessler, 2016; Im et al., 2011; Kidani et al., 2013; Liu et al., 2013; York et al., 2015). In contrast, under homeostatic conditions, SREBPs can have suppressive functions, including restraining the basal type I IFN response and spontaneous pyrin inflammasome activity, and SREBP1 can promote resolution of inflammatory responses by inducing enzymes that synthesize suppressive unsaturated FAs (Akula et al., 2016; Oishi et al., 2017; Park et al., 2016; York et al., 2015). Although the mechanisms by which SREBP regulates immune cell activation and function are not fully understood, a common theme is that by altering cellular levels of cholesterol, its incorporation into membranes, and its metabolites, SREBPs affect organelle biogenesis, the physical and signaling properties of various membranes, stress responses, and membrane-signaling protein interactions (Akula et al., 2016; Bekkering et al., 2018; Dang et al., 2017; Fessler, 2016; Park et al., 2016; York et al., 2015). The complex and context-dependent immune functions of SREBPs are typically attributed to their effects on cellular metabolism, primarily generation of sterols.

Macrophages are innate immune cells that orchestrate inflammation, immune responses, and tissue repair (Ginhoux et al., 2016). Macrophages polarize into various functional states in response to environmental cues (Glass and Natoli, 2016; Lawrence and Natoli, 2011; Murray, 2017). IFN-g, microbial products, TNF and type I IFNs polarize macrophages towards classical inflammatory (M1-like) states that are important for host defense but have tissue-destructive properties. IL-4, IL-13, IL-10 and glucocorticoids polarize macrophages towards alternative and pro-resolution (M2-like) states that promote tissue repair. Macrophages play a key role in the repair of skin wounds (Goren et al., 2009; Lucas et al., 2010; Marshall et al., 2018; Minutti et al., 2017; Wynn and Vannella, 2016). TNF-exposed macrophages drive the inflammatory early phases of wound repair, while at later stages macrophages manifest a pro-resolution phenotype that dampens inflammation and promotes angiogenesis, new tissue formation and maturation (Eming et al., 2007; Eming et al., 2017;

Marshall et al., 2018). Perturbation of this transition to a pro-resolution macrophage phenotype is detrimental to the healing process (Knipper et al., 2015). In line with this, pathological non-resolving wounds in chronic inflammatory disorders display an aberrant tissue repair program, in which excessive TNF activity perpetuates macrophage inflammatory responses and impedes the emergence of the resolution phase (Kroner et al., 2014; Sindrilaru et al., 2011; Streit et al., 2006; Teich and Klugmann, 2014).

We wished to identify mechanisms that regulate the late phase macrophage response to TNF and can be targeted to modulate TNF-induced macrophage polarization to alleviate inflammatory pathology and promote wound healing. An epigenomic analysis of the TNF response in primary human macrophages revealed late phase activation of SREBP2 activity. In addition to activating its canonical cholesterol target genes, SREBP2 bound to various inflammatory and interferon response genes and promoted TNF-induced inflammatory polarization independently of its functions in sterol metabolism. Ablation of SREBP function by deletion of its chaperone SCAP shifted the balance of macrophage polarization from inflammatory to pro-resolution in *in vivo* peritonitis and skin wound healing models. Conditional deletion of *Scap* in myeloid cells or topical pharmacological inhibition of SREBP improved skin wound healing under homeostatic and chronic inflammatory conditions. Our results identify a function and mechanism of action for SREBP2 in promoting inflammation, and open avenues for therapeutically modulating macrophage polarization to promote wound repair.

RESULTS

SREBP-cholesterol synthesis pathway is induced at a late phase by TNF in human macrophages

We analyzed the later phase of the TNF response using RNA sequencing (RNA-seq) of primary human macrophages exposed to TNF for 24 hours (herein termed the ‘late phase response’). TNF stimulation significantly ($p < 0.01$) upregulated expression of 951 genes and downregulated expression of 1041 genes (Figure 1A). Pathway analysis of differentially expressed genes (DEGs) showed that pathways most significantly induced by TNF at 24 hr were substantially different from those induced at 3 hr (Park et al., 2017) (Figure 1B and S1A). As expected, 3 hr of stimulation with TNF most significantly activated genes in pathways related to host defense and inflammatory signaling (Figure S1A). In contrast, 24 hr of TNF stimulation most significantly induced genes in cholesterol biosynthesis pathways, although inflammatory and interferon response genes were also induced as previously described (Park et al., 2017; Yarilina et al., 2008) (Figure 1B-E). Bioinformatic analysis to identify upstream regulators of the late phase TNF response revealed the expected regulators NF-κB, STAT, IRF and AP-1, but also suggested that TNF activates SREBP transcription factors that are master inducers of cholesterol biosynthesis, while inhibiting INSIGs, which are inhibitors of SREBP (Figure 1C). In line with these results, *de novo* motif analysis of promoters of genes induced after 24 hr of TNF stimulation revealed enrichment of binding sites for SREBP, in addition to the expected NF-κB, IRF and AP-1 proteins (Figure S1B). Induction of representative inflammatory, IFN response and cholesterol pathway late phase TNF response genes is displayed in a heat map in Figure 1D; 20 out of 22 genes in the core

cholesterol biosynthesis pathways were induced by TNF (Figure 1D, S1C and data not shown). Induction of key cholesterol pathway genes by TNF was confirmed in multiple donors by qPCR (Figure 1E). Induction of these genes peaked at 10 ng/ml of TNF, which concentration was used for the remainder of our study (Figure S1D).

These results indicate that a major component of the late phase TNF response is induction of SREBP target genes that comprise the cholesterol biosynthetic pathway, and suggest that TNF may activate SREBP. Accordingly, TNF induced expression of SREBP2 mRNA (Figure 1F) and substantially increased nuclear amounts of the activated form of SREBP2 (N-SREBP2) (Figure 1G). A time course experiment supported a role for SREBP2 in the late phase TNF response (Figure S1E). Finally, TNF increased cellular amounts of cholesterol (Figure 1H). Collectively, the results show that TNF induces a complex late phase response that includes sustained expression of select inflammatory and interferon response genes, and an SREBP-cholesterol axis, in human macrophages. This axis appears to be operative in chronic TNF-driven inflammatory states, as rheumatoid arthritis (RA) joint macrophages exhibited increased expression of SREBP2 and cholesterol pathway genes (Figure 1I and S1F).

TNF regulates chromatin states at cholesterol pathway genes

To gain insight into mechanisms that regulate different components of the late phase TNF response, we analyzed the genome-wide profile of chromatin accessibility and various histone marks using our epigenomic data set generated using ATACseq and ChIPseq (GSE100383 and GSE129229). In contrast to immune response genes that were associated with TNF-induced chromatin accessibility and increases in multiple positive histone marks (Park et al., 2017; Tong et al., 2016), genes in the cholesterol pathway exhibited open chromatin and positive histone marks at baseline, which increased minimally if at all upon TNF stimulation (Figure 1J, S2A, and data not shown). One exception was TNF-induced increase in ubiquitination of the histone H2BK120 (H2Bub), a positive mark associated with promoter activation and gene transcription (Figure 1J; representative gene tracks shown in Figure S2B).Thus, expression of inflammatory and cholesterol pathway genes is associated with different patterns of chromatin remodeling, consistent with differential baseline gene expression.

We reproduced previous work in other systems showing that addition of exogenous type I IFNs inhibits cholesterol pathway genes (Blanc et al., 2011; Dang et al., 2017; Reboldi et al., 2014; York et al., 2015), and further found that type I IFNs suppressed H2Bub at the cholesterol pathway gene set (Figure S2C and S2D). However, the small amounts of endogenous IFN produced in this system (Yarilina et al., 2008) were insufficient to suppress cholesterol pathway gene expression (Figure S2E). Investigation of additional pathways and transcription factors that may regulate cholesterol pathway genes implicated AP-1 proteins, with enrichment of AP-1 binding motifs analysis under TNF-inducible ATAC-seq peaks and induction of several AP-1 family members (Figure 1K, S2F and S2G). Accordingly, inhibition of the MAPK-AP-1 pathway selectively during the late phase TNF response attenuated expression of SREBP2 and cholesterol pathway genes (Figure S2H). These results suggest that the canonical TNF-induced MAPK-AP-1 signaling pathway, likely

working in cooperation with SREBP (see below), is important for cholesterol pathway gene induction.

SREBP2 promotes TNF-induced inflammatory macrophage activation independently of cholesterol

We used a combination of pharmacologic and genetic loss- and gain-of-function approaches to investigate the role of SREBP2 in the late phase TNF response. We first inhibited SREBP2 activation using exogenous cholesterol or fatostatin, which inhibits SREBP translocation to the Golgi (Figure 2A). We confirmed that both inhibitors suppressed TNF-mediated induction of canonical cholesterol pathway genes (Figure 2B and S3A). Screening RNA-seq experiments showed that in addition to inhibiting cholesterol pathways, both inhibitors significantly attenuated TNF-induced activation of inflammatory and IFN response pathways and genes (Figure S3B and S3C, left two panels). Attenuation of TNF-mediated induction of canonical inflammatory and IFN response genes such as *GBP1*, *IL8* and *CCL5* by cholesterol and fatostatin was confirmed by qPCR (Figure 2C, representative genes). Similar results were obtained using a third chemically unrelated inhibitor betulin which acts immediately upstream of SREBP by stabilizing interactions with the negative regulator INSIG (Figure 2A and 2D). Furthermore, similar decreases in cholesterol pathway and inflammatory gene expression were observed when SREBP2, but not SREBP1, expression was knocked down using short interfering RNAs (Figure 2E and S3D). These results suggest an augmenting effect of SREBP2 on inflammatory and IFN response components of TNF-induced macrophage polarization.

To corroborate these results we took the complementary approach of forced expression of a FLAG-tagged mature SREBP2 fragment (N-SREBP2), which localizes to the nucleus and is constitutively active, in primary human macrophages using adenoviral-mediated transduction. Relative to control macrophages transduced with adenoviral particles encoding eGFP, this approach achieved modest increases in *SREBF2* mRNA and exogenous N-SREBP2 protein, which were less than the amounts of endogenous protein (Figure 2F and 2G). As expected, increased N-SREBP2 expression resulted in increased expression of its cholesterol pathway canonical target genes *DHCR24* and *LDLR* (Figure 2H). N-SREBP2 also increased expression of IFN response genes in the absence of TNF stimulation, and superinduced their expression under TNF-stimulated conditions (Figure 2H). Collectively, the combination of SREBP2 loss-and gain-of-function experiments strongly supports the conclusion that SREBP2 plays a role in augmenting inflammatory and IFN-mediated components of the late phase TNF response, thus supporting SREBP2 as a transcriptional mediator of inflammatory macrophage activation.

We next addressed the possibility that SREBP was exerting its effects on inflammatory and IFN response gene expression via increased synthesis of cholesterol or pathway intermediates. To this end, we added atorvastatin, which inhibits *de novo* synthesis of cholesterol and pathway intermediates by inhibiting HMGCR, an enzyme upstream in the cholesterol synthesis pathway (Figure 2A and S1C), to cells transduced with N-SREBP2. Consistent with existing literature, there was an upward trend in *LDLR* expression after atorvastatin addition to N-SREBP2 transduced macrophages (Figure 2I), most likely related

to increased activity of endogenous SREBP2 upon cholesterol depletion. More importantly, atorvastatin did not suppress, and instead showed a trend towards increasing, N-SREBP-mediated induction of inflammatory and IFN response genes (Figure 2I and S3C, right panel). Similar results were obtained using nontransduced macrophages (Figure S3E). These results exclude that induction of inflammatory and IFN response genes by SREBP2 is mediated via increased synthesis of cholesterol or pathway intermediates, although decreased production of suppressive cholesterol pathway intermediates may contribute (Akula et al., 2016; Park et al., 2016). Overall, the results support a role for SREBP2 in inflammation that is independent from its conventional function as a regulator of cellular cholesterol synthesis.

SREBP2 binds to TNF late phase inflammatory and IFN response genes

Since we uncoupled SREBP2 induction of TNF late phase inflammatory and interferon response genes from its role in cholesterol biosynthesis, we wondered whether SREBP2 promotes expression of these genes directly through its function as a transcriptional activator. We conducted an integrated RNA-seq and ChIP-seq analysis using cells transduced with FLAG-tagged N-SREBP2. Forced expression of N-SREBP2 in the context of adenoviral transduction of primary human macrophages resulted in upregulation of 682 genes ($p < 0.05$), with minimal gene repression (Figure 3A). IPA analysis revealed that N-SREBP2 activated genes associated with inflammatory (TNF, IL-1, NF-κB), interferon, and cholesterol synthesis pathways (Figure 3B and 3C). We also observed superinduction of inflammatory, interferon and cholesterol pathway genes by N-SREBP2 under TNF-stimulated conditions (Figure S4A and S4B).

Next, we used ChIP-qPCR and ChIP-seq to assess SREBP2 binding to target genes in resting or TNF-stimulated macrophages. TNF treatment increased the binding of endogenous SREBP2 to cholesterol pathway, inflammatory, and interferon response gene regulatory elements (Figure S4C). We performed ChIP-seq with macrophages transduced with FLAG-tagged N-SREBP2, which enabled us to take advantage of the exquisite specificity and high affinity of FLAG antibodies under conditions of near-physiological amounts of SREBP2. Pilot ChIP-qPCR experiments for FLAG-N-SREBP2 binding showed virtually no background binding and specific occupancy of *HMGCR*, *LDLR*, *IL1B,* and *CXCL10* regulatory regions, which increased after TNF stimulation (Figure S4D). Subsequent ChIP-seq analysis revealed that FLAG-N-SREBP2 bound to 19,990 sites and the amount of binding and the numbers of binding sites were increased to 31,474 by TNF stimulation (Figure 3D). Occupancy of SREBP2 binding sites was highly correlated with SREBP2-inducible gene expression (Figure 3E), and gene ontology pathway analyses showed SREBP2 binding sites are significantly associated with inflammatory and interferon response genes (Figure 3F). SREBP2 binding was highly enriched at promoters and introns that represent a small fraction of the genome (Figure S4E), which is consistent with previous ChIP-seq analysis of SREBP occupancy in other cell types (Reed et al., 2008; Seo et al., 2009; Seo et al., 2011). Representative gene tracks of SREBP2 binding are shown in Figure 3G and S4F. These results indicate that SREBP2, which is induced and activated by TNF, broadly binds to regulatory elements in late phase TNF response genes and is associated with their increased expression.

To gain insight into determinants of SREBP2 binding, we performed *de novo* motif analysis of sequences under SREBP2 peaks genome-wide. We found enrichment of SREBP motifs (termed SREs), suggestive of direct binding to DNA, and NFY motifs, consistent with coordinate binding in other cell types (Figure 3H) (Reed et al., 2008; Seo et al., 2009; Seo et al., 2011). TNF induced SREBP2 binding to regions enriched for the Fra1-variant AP-1 motif, for E box elements to which SREBP binding has been previously described (Kim et al., 1995) (Reed et al., 2008; Seo et al., 2009; Seo et al., 2011), and for NF-κB and ISRE motifs (Figure 3H and S4G). Motif enrichment analysis found significant enrichment of AP-1, NF-κB, NFY, E box and SREBP2 motifs associated with inflammatory genes (n = 200) and AP-1 and IRF sites associated with IFN response genes (n = 97) (Figure S5A and S5B); direct sequence inspection revealed that 59% of IFN response genes had an associated CANNTG core E box motif. E boxes have been previously implicated in regulation of inflammatory gene expression (Hu et al., 2008; Sharif et al., 2006; Sosic et al., 2003). These results suggest that the altered genomic profile of SREBP2 binding after TNF stimulation is mediated at least in part by an alternative mode of SREBP2 binding to inflammatory and IFN response genes. This binding may occur via lower affinity interactions with E boxes or indirect binding in cooperation with TNF-induced AP-1, NF-κB and STAT/IRF factors. Consistently, the amount of SREBP2 binding to inflammatory and IFN response genes was lower than to canonical cholesterol pathway genes, but substantially higher than to control non-TNF-inducible genes (Figure S4C, S4D and S5C). SREBP2 binding peaks most highly induced by TNF were enriched in NF-κB, Fra1 and SREBP motifs and associated with inflammatory pathways (Figure S5D-5F). Collectively, the data suggest that in the setting of TNF stimulation SREBP2 is induced, activated, and can cooperate with other TNF-induced transcription factors to drive gene transcription, including inflammatory and IFN response genes.

Inactivation of SREBP function in mouse macrophages shifts TNF-induced polarization towards alternative activation

As deletion of SREBP genes has resulted in compensation by the other isoform (Horton et al., 2002), we tested the role of SREBP in murine macrophages using the standard approach of targeting SREBP cleavage-activating protein (SCAP), whose deletion renders cells unable to activate SREBP (Matsuda et al., 2001). We developed mice with myeloid specific deficiency of SCAP by crossing LysM-Cre mice with *Scap*$^{fl/fl}$ mice (hereafter: *Scap*$^{fl/fl}$ LysM-Cre) and used LysM Cre, *Scap*$^{+/+}$ littermates as controls. Deficiency of SCAP resulted in decreased TNF-induced expression of cholesterol pathway and inflammatory genes in zymosan-elicited peritoneal macrophages stimulated *ex vivo* with TNF (Figure 4A and 4B). Consistent with a decreased classical inflammatory response, freshly isolated macrophages from *Scap*$^{fl/fl}$ LysM-Cre mice subjected to the chitin-induced peritonitis *in vivo* model of alternative activation (also termed M(IL-4) polarization) (Murray, 2017) (Satoh et al., 2010) showed elevated expression of M(IL-4) genes such as *Retnla*, *Arg1*, *Chil3, Mrc1 and Cd163* relative to control macrophages (Figure 4C). This increase in M(IL-4) gene expression could be attributed in part to increased gene induction in response to IL-4 (Fig. S5G and S5H). Taken together, the results suggest that *Scap* deletion shifts the balance from inflammatory towards alternative M(IL-4) macrophage polarization.

Myeloid SREBP activity suppresses epidermal and dermal wound-healing

As effective skin wound healing depends upon the balance and shift from an inflammatory to a reparative macrophage phenotype (Knipper et al., 2015), we tested the effects of myeloid *Scap* deletion on tissue repair using a full thickness dorsal excisional skin wound model. There were no detectable differences in unwounded skin between $Scap^{fl/fl}$ LysM-Cre and control mice (Figure S6A). After wounding, we tracked the progress of healing over 6 days through daily time-lapse photographs and planimetric measurements. Wounds from $Scap^{fl/fl}$ LysM-Cre mice closed at a highly significantly accelerated pace, compared with controls (Figure 5A and 5B). Histological analyses revealed enhanced epithelialization of wounds in $Scap^{fl/fl}$ LysM-Cre mice 4 and 6 days post injury (dpi), signifying accelerated healing (Figure 5C and 5D). Blinded pathological assessment of epithelialization showed consistently and significantly higher epithelialization scores in $Scap^{fl/fl}$ LysM-Cre mice across all time points tested (Figure 5E).

Additionally, we explored the role of SREBP in the tissue granulation process. Immunohistochemical staining for CD31, a marker of endothelial cells, showed that wounds from $Scap^{fl/fl}$ LysM-Cre mice have extensive CD31 staining in the tissue granulation area at 6 dpi, with a portion of this CD31 positive region starting to form elongated and branched structures that resemble capillary vasculature (Figure 5F). In contrast, wounds from control mice at 6 dpi were only positive for CD31 staining at the wound edge and a proportion of the positive cells stained as singlets, indicating that they are in the initial stage of angiogenesis (Figure 5F). Another event that defines tissue granulation is myofibroblast-mediated wound contraction. Smooth Muscle Actin (SMA) staining to label myofibroblasts in the healing skin tissue revealed similar localization and quantity of SMA+ cells in $Scap^{fl/fl}$ LysM-Cre mice and controls. However, closer examination revealed that SMA+ cells from $Scap^{fl/fl}$ LysM-Cre mice were mostly in a spindle-like shape that resembles mature myofibroblasts and were positioned parallel to the migrating keratinocytes, which ultimately aids horizontal wound contraction. In contrast, a portion of SMA+ cells from control mice exhibited a rounded form and was more haphazardly oriented, signifying the more primordial nature of myofibroblast differentiation (Figure 5G). Cumulatively, our data suggest that loss of SREBP function in the myeloid compartment leads to an accelerated skin repair program, both in the epidermis and dermis.

It is possible that effects of SCAP deficiency on the amounts of cellular cholesterol and fatty acids and thus macrophage lipid metabolism contribute to the observed phenotypes. Arguing against this possibility is data in two previous reports (Guo et al., 2018; York et al., 2015) that SCAP-deficient macrophages have normal amounts of cellular lipids, which we reproduced in our system (Figure S6B). This is most likely explained by the ability of macrophages to take up extracellular lipids and cholesterol. We experimentally addressed the possibility that suppressed lipid production could contribute to the observed wound healing phenotype using local application of inhibitors of fatty acid and/or cholesterol synthesis. Opposite to the effects of SCAP deficiency, none of the three inhibitors accelerated skin wound closure, and instead had either no effect or delayed wound healing (Figure S6C-S6H). Additionally, dietary intervention that abrogated production of pro-resolution essential omega fatty acids that is mediated by SREBP1 (Ander et al., 2003; Oishi

et al., 2017) had no effect on skin wound healing, suggesting that pro-resolution fatty acid synthesis does not play a major role in modulating skin reparative response (Figure S6I, S6J). Collectively, the data argue against alterations in lipid synthesis as a major explanation for our findings, but this possibility merits further investigation.

SREBP regulates infiltration and phenotype of skin wound macrophages

We next determined whether SCAP deficiency resulted in changes in the numbers or phenotype of wound macrophages that could potentially explain accelerated healing. Published work shows that higher accumulation of macrophages and expression of an M2-like reparative phenotype are associated with accelerated and superior tissue repair (Hu et al., 2017; Knipper et al., 2015). We FACS-sorted (gating strategy shown in Figure S6K) cells obtained from wounds of *Scap*$^{fl/fl}$ LysM-Cre and control mice at the peak of the inflammatory phase, 4 dpi. In the CD45+ hematopoietic cell fraction, the majority of cells fell into two populations, CD11b+ F4/80+ double positive cells (DP cells) and CD11b+ F4/80- single positive cells (SP cells) (Figure 6A). The CD11b+ F4/80+ cells correspond to macrophages and the CD11b+ SP cells are also myeloid lineage as they were mostly CD3- B220- NK1.1- Ly6C+ Ly6G+ (Figure S6L). Expression of the canonical SREBP target gene *Dhcr24* was comparably decreased in DP and SP cells (Figure S6M), thus verifying SREBP loss of function. Flow cytometric quantitation of sorted cells from wounds showed significant elevation in total CD45+ cells in *Scap*$^{fl/fl}$ LysM-Cre wounds, which was mainly due to an increase in DP macrophages (Figure 6A). Thus, *Scap*$^{fl/fl}$ LysM-Cre wounds are characterized by higher numbers of macrophages, which has been previously associated with improved healing.

We next analyzed the functional phenotype of day 4 dpi wound-infiltrating macrophages using single cell RNA-seq. Single cells were clustered based on gene expression using Seurat (https://satijalab.org/seurat/) and visualized using a tSNE plot (Figure 6B) or a heat map (Figure 6C). The macrophages clearly separated into 2 major clusters, which corresponded to DP cells (Figure 6B, upper, comprised of sub-clusters C0 and C3) and SP cells (Figure 6B, lower, comprised of sub-clusters C1 and C2). DP macrophages, which were increased in number in *Scap*$^{fl/fl}$ LysM-Cre wounds, expressed genes indicative of an M2-like reparative phenotype, including *Mrc1*, *Arg1*, *Vegfa*, and *Cd36*, while SP cells expressed inflammatory genes such as *Il1b*, *Tnf*, and *Irg1* (Figure 6B-D and S7A). Thus, at the early 4 dpi time point there are increased numbers of macrophages with a reparative phenotype in *Scap*$^{fl/fl}$ LysM-Cre wounds. During the later tissue granulation phase at 6 and 8 dpi, DP wound-infiltrating macrophages from *Scap*$^{fl/fl}$ LysM-Cre mice exhibited elevated expression of *Tgfb1*, *Vegfa*, *Mrc1* and *Cd163*, and decreased expression of *Cxcl10* as measured by qPCR (Figure 6E, S7B). Thus, *Scap*-deficient wound macrophages exhibit higher expression of reparative M2-like genes. Overall, the results support the notion that SCAP deficiency in macrophages results in elevated expression of genes that encode proteins that can promote tissue repair by acting on endothelial cells and myofibroblasts, and possibly by additional mechanisms.

Topical inhibition of SREBP accelerates wound healing under homeostatic and chronic inflammatory conditions

To explore the translational implications of our findings, we tested the effects of local SREBP inhibition on skin wound healing under homeostatic and inflammatory conditions. First, we inflicted bilateral dorsal symmetrical excisional skin wounds and subsequently topically applied control ointment or ointment containing the SREBP inhibitor betulin (Figure 2A) to one of the two wounds in each mouse (Figure 7A). Similar to the effects of *Scap* deletion, betulin treatment accelerated wound closure (Figure 7B and 7C). Histological examination showed that betulin accelerated the healing and re-epithelialization processes (Figure 7D and 7E), angiogenesis (Figure 7F), and maturation of myofibroblasts (Figure 7F). Thus, the effects of local SREBP inhibition phenocopy those of myeloid SREBP inactivation on the improvement of skin wound healing. Collectively, our data suggest that myeloid deletion or local inhibition of SREBP accelerate healing in both epidermis and dermis by promoting epithelialization, angiogenesis, and myofibroblast-induced wound contraction.

Patients with chronic wounds or inflammatory disorders display aberrant tissue repair where the inflammatory phase is sustained and the resolution phase is impeded. In addition, TNF accumulation in wounds is associated with poor healing (Kroner et al., 2014; Sindrilaru et al., 2011; Streit et al., 2006; Teich and Klugmann, 2014). To model the effects of chronic inflammation on wound healing, we used TNF transgenic (TNF-Tg) mice, which constitutively express a human TNF transgene and are exposed to long-term systemic TNF inflammatory action. TNF-Tg mice had normal skin at baseline (Figure S7C) but exhibited a significant delay in wound closure (Figure S7D and S7E) and epithelialization rate (Figure S7F and S7G). Thus, TNF-Tg mice model the defective wound healing process observed in patients with chronic inflammatory disorders. We then asked whether topical SREBP inhibition using betulin ointment could accelerate and potentially normalize this defective healing process. Betulin ointment substantially accelerated wound closure in TNF-Tg mice relative to control ointment applied to contralateral wounds (Figure 7G and 7H). Betulin-treated wounds showed more advanced healing upon histological analysis (Figure 7I), increased epithelialization (Figure 7J), and accelerated angiogenesis and myofibroblast differentiation (Figure 7K). These results show, using a therapeutic design, that topical SREBP inhibition can accelerate skin wound healing under pathological inflammatory conditions.

DISCUSSION

TNF-induced macrophage polarization underlies chronic inflammatory pathology in many autoimmune diseases (Kalliolias and Ivashkiv, 2016). Although the early phase inflammatory response encompassing the first minutes to approximately 3 hours of TNF stimulation is well understood (Aggarwal, 2003; Brenner et al., 2015; Kalliolias and Ivashkiv, 2016), less is known about later phase responses that are important for macrophage polarization and disease pathogenesis. In this study we have identified an SREBP2-driven transcriptional response as a component of the late phase TNF response in macrophages, and linked SREBP2 to classical inflammatory polarization working by a transcriptional

mechanism that is independent of its role in cholesterol metabolism. The function of SREBP in macrophage polarization is (patho)biologically important, as expression of its target genes is elevated in RA macrophages, and genetic or pharmacological modulation of SREBP activity resulted in improved wound healing associated with a shift in macrophage polarization towards a reparative phenotype. These findings identify a function for SREBP2 in regulating the balance of macrophage polarization and open therapeutic avenues towards improving wound healing, including healing of chronic inflammation-associated wounds.

The importance of cellular metabolism in immune cell function has been clearly established (O'Neill et al., 2016). The predominant model in the immunometabolism field is that metabolites generated during cell activation play important roles in cell expansion and/or effector function. In accord with this model, SREBPs have been shown to exert effects on immune cells via production of cholesterol pathway intermediates, cholesterol itself, and cholesterol-derived oxysterols (Akula et al., 2016; Bekkering et al., 2018; Dang et al., 2017; Fessler, 2016; Liu et al., 2013; Park et al., 2016; Reboldi et al., 2014; Spann et al., 2012; Wei et al., 2016; York et al., 2015). One common aspect of previously described mechanisms is that sterols mediate the effects of SREBP on immune function by altering membrane lipid composition that affects signaling or stress responses, or by binding to specific cellular receptors (Fessler, 2016). In contrast, we have uncovered a mechanism of SREBP2 action that is independent of sterol metabolism, but instead is mediated by direct binding and transcriptional activation of inflammatory and interferon response genes. It is possible and actually likely that effects of SCAP deletion on cellular lipid metabolism contribute to the phenotypes we have observed. A caveat of our study is that we did not analyze deletion of SREBP2 alone; although such studies can be complicated by compensation by one SREBP isoform when the other is deleted, dependence of SREBP1c expression on SREBP2, and uptake of extracellular lipids (Liang et al., 2002; Rong et al., 2017; Shimano et al., 1997), this is an important question to address in future work. Overall, the final outcome of SREBP activity on macrophage phenotype will be determined by integration of the effects of sterols, lipid metabolism, and the noncanonical transcriptional pathway described herein.

Under non-inflammatory conditions in macrophages, low amounts of N-SREBP2 maintain cholesterol pathway gene expression, similar to other cell types, and the predominant functions of SREBP2 are likely mediated by sterol metabolites. Stimulation with TNF increased nuclear amounts of N-SREBP2 and altered its genomic binding profile to include inflammatory and IFN response genes. In line with these findings, a recent study identified an increase in LPS-induced inflammatory response due to an overexpression of SCAP in THP1 cells (Ouyang et al., 2018). The altered genomic profile of SREBP occupancy after TNF stimulation is likely explained in part by increased nuclear concentrations of N-SREBP2 that promote binding to lower affinity E boxes, and also likely by cooperation with other TNF-induced transcription factors (TFs). A model whereby TNF stimulation alters the genomic profile of SREBP2 occupancy can explain context-dependent function of SREBP2, such as suppression of basal ISG expression in resting mouse macrophages (York et al., 2015) *versus* superinduction of inflammatory genes and ISGs in TNF-stimulated human macrophages.

Macrophage polarization in response to TNF needs to be balanced to preserve host defense while avoiding toxicity related to excessive inflammation (Eming et al., 2014; Medzhitov, 2008; Nathan and Ding, 2010; Wynn and Vannella, 2016). Emerging evidence supports that such balanced polarization is achieved by integration of opposing feed-forward and feedback inhibitory mechanisms, such as autocrine IFN-STAT1 and IL-10-STAT3 loops, and regulation of chromatin accessibility (Park et al., 2011; Yarilina et al., 2008) (Huynh et al., 2016) (Park et al., 2017). In this study, we have added SREBP-mediated transcriptional responses as a key component of TNF-induced macrophage polarization that promotes inflammatory and IFN responses. In accord with a pro-inflammatory role, SREBP2 was recently shown to form tertiary complexes with SCAP and NLRP3 to regulate inflammasome activation and IL-1 production (Guo et al., 2018). However, IL-1 blockade had no effect on inflammatory gene expression (data not shown), indicating that inflammasome activation did not contribute to gene induction in our system. TNF-induced SREBP activity also can increase expression of cholesterol pathway genes in inflammatory settings such as RA and may contribute to macrophage foam cell formation observed in atherosclerosis (Li et al., 2013; Spann et al., 2012; Tall and Yvan-Charvet, 2015).

One aspect of our model is that each component of the late phase TNF response can be independently regulated, for example by exogenous cytokines (type I IFNs, IL-10) produced by other cells, and by nutrient availability and metabolic status that determines cellular amounts of cholesterol and SREBP activity. Thus, the functional outcome of TNF-mediated macrophage polarization can be fine tuned to match environmental conditions. Our model extends a generally accepted conceptualization of macrophage polarization (Murray et al., 2014) that highlights the importance of individual cytokines in polarizing macrophages towards a defined phenotype. That paradigm recognizes the complexity of macrophage polarization *in vivo* but places it predominantly in a conceptual framework of cooperative and opposing activities of factors present in inflammatory environments, with the idea that any individual factor induces a stereotypical polarization phenotype (for example, M(IFN-g) or M(IL-4)). Such opposing activities are important in counterbalancing the effects of TNF and IL-13 in tumor macrophages (Kratochvill et al., 2015). Our model extends this concept by highlighting the plasticity of polarization in response to one cytokine TNF, which will be modulated not only by environmental influences but also by nutritional status and genetic variability amongst individuals. The output of cholesterol biosynthetic pathways (conventionally measured as serum cholesterol) has a strong genetic component (Helgadottir et al., 2016), and gene regulatory elements that mediate IFN responses harbor amongst the highest allelic variation (Maurano et al., 2012). Thus, variability in TNF-mediated macrophage polarization amongst individuals may help explain differences in disease susceptibility or progression.

Our findings that genetic or pharmacological suppression of SREBP activity accelerates skin wound healing have clear translational implications for treatment of non-healing or chronically inflamed wounds. We investigated the role of SREBP in the well characterized skin wound model, where a transition from an early inflammatory response to a reparative response plays a key role in healing (Eming et al., 2007; Eming et al., 2017; Knipper et al., 2015). In skin wounds, deficiency in myeloid SREBP activity resulted in diminished M1-like polarization and concomitant increased polarization towards an M2-like phenotype.

Single cell RNA sequencing suggested that at an early stage 4 dpi, enhanced M2-like polarization occurs at least in part because of increased infiltration by F4/80+ CD11b+ DP macrophages that express reparative genes. Increased numbers of these F4/80+ CD11b+ macrophages indicates an accelerated transition towards a reparative environment in skin tissue. The experimental approaches used do not allow us to determine whether there this occurs by a switch in phenotype of infiltrating macrophages, or by increased M2-like polarization of newly migrating monocytes; these possibilities are not mutually exclusive and will be investigated in future work. At the later phases of wound healing (6 and 8 dpi) purified DP macrophages from wounds in SREBP-defective mice clearly showed increased expression of reparative genes in association with accelerated tissue repair.

Although an early transient inflammatory response is integral for skin wound healing, a prolonged and sustained inflammatory response suppresses the healing process (Marshall et al., 2018; Perretti et al., 2017; Wynn and Vannella, 2016; Zhao et al., 2016). Indeed, macrophages that exhibit a prolonged inflammatory phenotype are detrimental to the wound healing process (Chen et al., 2012; Kroner et al., 2014; Sindrilaru et al., 2011). These observations help explain the defective wound healing that is one of the key clinical features of chronic TNF-mediated autoimmune disorders (Nathan and Ding, 2010; Streit et al., 2006; Teich and Klugmann, 2014). The substantial improvement in delayed wound healing in TNF-Tg mice after topical application of betulin suggests inhibition of SREBP may represent a promising approach to treatment of non-healing skin wounds. As other inflammatory lesions, such as synovitis in RA (Firestein and McInnes, 2017; Perretti et al., 2017) or plaque inflammation in atherosclerosis (Tabas and Lichtman, 2017) have been proposed to represent non-healing wounds, it is tempting to speculate that SREBP inhibition may be efficacious in treatment of various inflammatory lesions characterized by a sustained M1-like response that does not transition to a resolution phase. Betulin is a natural compound found in birch tree bark that was recently approved by the European Medicines Agency for treating split-thickness and second-degree burns (Dehelean et al., 2012), and additional SREBP inhibitors are under development for the treatment of hypercholesterolemia (Soyal et al., 2015); thus it may be straightforward to repurpose these drugs for treatment of chronic wounds and inflammatory lesions.

In summary, our findings identify SREBP as a key mediator of the TNF response and inflammatory macrophage polarization. Suppression of SREBP activity enables differentiation of macrophages towards a reparative phenotype and promotes tissue repair. These results provide a mechanism that regulates macrophage polarization and function, and open therapeuric avenues towards accelerating wound closure and tissue repair.

STAR METHODS

CONTACT FOR REAGENT AND RESOURCE SHARING

Further information and requests for resources and reagents should be directed to and will be fulfilled by the Lead Contact, Lionel B. Ivashkiv (ivashkivl@hss.edu).

EXPERIMENTAL MODEL AND SUBJECT DETAILS

Mice—LysM Cre male and female mice were crossed with *Scap*$^{fl/fl}$ mice to generate either LysM Cre *Scap*$^{fl/fl}$ or LysM Cre *Scap*$^{+/+}$ mice as littermate controls. 11–14 week old female mice were randomly assigned for wound healing experiment, while 11–14 week old male mice were randomly allocated to generate elicited peritoneal macrophages. C57BL/6J female mice were obtained from Jackson Laboratory and were randomly allocated for experiments using topical medication application at the age of 12 weeks. Six to eight week old female TNF transgenic mice and their respective controls were purchased from Taconic Farms and no treatments were given prior to the experiment. The wound healing and therapeutic experiments were performed when the randomly assigned TNF transgenic mice and their controls reached 12–14 weeks of age. Animals were housed in a specific pathogen-free environment in the Weill Cornell Medicine vivarium and all the experiments conformed to the ethical principles and guidelines approved by the Institutional and Animal Care and Use Committee of Weill Cornell Medical College.

For the modified fatty acid diet experiment, mice were fed *ad libitum* with either essential fatty acid (EFA) deficient or control diet (Envigo) for 2 weeks prior to infliction of skin wounds and maintained on the same diet during the entire healing process. EFA deficient diet contains regular fat content, but lacks essential omega fatty acids and their precursors, linoleic acid and alpha-linolenic acid.

Human cells—De-identified blood leukocyte preparations (buffy coats) were purchased from the New York Blood Center using a protocol approved by the Hospital for Special Surgery Institutional Review Board. The samples were anonymous and the investigators do not have access to any identifiable private information. As per the guidelines on Human Subjects Research in the PHS SF424 (R&R) Application Guide and underlying documentation, work with purchased de-identified blood products does not constitute human subjects research; informed consent was not obtained at Hospital for Special Surgery. Peripheral blood mononuclear cells (PBMCs) were separated by density gradient centrifugation with Ficoll (Invitrogen, Carlsbad, CA, USA) and monocytes were purified from PBMCs immediately after isolation by positive selection with anti-CD14 magnetic beads, as recommended by the manufacturer (Miltenyi Biotec) (Huynh et al., 2016). Monocytes were cultured at 37^{o}C, 5% CO_2 in RPMI-1640 medium (Invitrogen) supplemented with 10% heat-inactivated defined FBS (HyClone Fisher), penicillin-streptomycin (Invitrogen), L-glutamine (Invitrogen) and 10 ng/ml human M-CSF. The duration and dose of each stimulus are described in the figure legends.

METHOD DETAILS

Isolation of peritoneal macrophages—Elicited peritoneal macrophages were isolated from peritoneal exudate cells (PECs). Peritoneal exudate cells (PECs) were obtained by lavaging the peritoneal cavity twice with 5 ml ice cold PBS. To isolate the peritoneal macrophages, the lavaged PECs were further purified by CD11b microbead positive selection following the instructions of the manufacturer (Miltenyi Biotec), followed by adherence selection in DMEM medium (supplemented with L-glutamine and Penicillin-Streptomycin). After 3 hours of culture cells that remained in suspension were removed by

aspiration and attached cells were washed once, then cultured with complete DMEM medium (10% heat inactivated FBS, penicillin-streptomycin, and L-glutamine). The purified cells were then harvested and processed for specific assays. The duration and dose of each stimulus are indicated in the figure legends.

Analysis of mRNA and protein—Total RNA was extracted with an RNeasy Mini Kit and was reverse-transcribed with a First Strand cDNA Synthesis kit (Fermentas). Real-time PCR was performed with Fast SYBR Green Master Mix and a 7500 Fast Real-time PCR system (Applied Biosystems). The primer sequences for the quantitative RT-qPCR reactions are listed on the key resource table.

Prior to cell harvest for protein analysis, 0.25% pefabloc was added to the cell culture for 5 minutes. Whole-cell extracts and nuclear extracts were fractionated by 7.5–10% SDS-PAGE, transferred to polyvinylide fluoride membranes (Millipore) and incubated with specific antibodies (identified on the key resource table), then enhanced chemiluminescence was used for detection (Amersham).

RNA sequencing—After RNA extraction, libraries for sequencing were prepared using the TruSeq RNA Library Preparation v2 Kit following the manufacturer's instructions (Illumina). Quality of all RNA and library preparations were evaluated with BioAnalyser 2100 (Agilent) and the sequencing input was 500 ng total RNA. High-throughput sequencing (50 bp, single-stranded) was performed at the Weill Cornell Medicine Genomic Core Facility, using cBot and HiSeq4000 (Illumina). The read depth was 30 to 50 million reads per sample.

Cholesterol quantitation—Total cholesterol content of human CD14+ macrophages was extracted by modified Folch method (Folch et al., 1957). We resuspended cell pellets in Chloroform:Methanol (2:1) solution, followed by incubation on a shaker for 30 minutes at room temperature. After incubation, the homogenized solution was centrifuged at 12,000 rpm for 5 minutes and the supernatant was extracted. Then, we added 0.9% NaCl solution to the supernatant at a ratio of 2:5. Once mixed, the samples were centrifuged for 3,000 rpm for 10 minutes and the lower layers were transferred and dried under 45^{o}C inert gas. The dried samples were resuspended with assay buffer and the cholesterol quantitation steps were performed, following the manufacturer's protocol (Thermo Scientific). Fluorescence intensity was measured with Varioskan Flash Spectral Scanning (Thermo Scientific) and cell number as quantitated with a hemocytometer (Fisher Scientific) was used for normalization.

ATAC sequencing—ATAC seq was performed using cultured primary human macrophages (Park et al., 2017). To prepare nuclei, we centrifuged 50,000 cells at 500*g* for 5 min, which was followed by a wash using 50 ml of cold PBS and centrifugation at 500*g* for 5 min. Cells were lysed using cold lysis buffer (10 mM Tris-HCl, pH 7.4, 10 mM NaCl, 3 mM MgCl2 and 0.1% IGEPAL CA-630). Immediately after lysis, nuclei were spun at 500*g* for 10 min in a refrigerated centrifuge. Immediately following the nuclei prep, the pellet was resuspended in the transposase reaction mix (25 μl 2× TD buffer, 2.5 μl transposase (Illumina) and 22.5 μl nuclease- free water). The transposition reaction was carried out for 30 min at 37 °C. Directly following transposition, the sample was purified using a MinElute

PCR Purification kit. Then, we amplified library fragments using 1× NEB next PCR master mix and 1.25 M of cust om Nextera PCR primers as previously described (Park et al., 2017), using the following PCR conditions: 72 °C for 5 min; 98 °C for 30 s; and thermocycling at 98 °C for 10 s, 63 °C for 3 0 s and 72 °C for 1 min. The libraries were purified using a Qiagen PCR cleanup kit yielding a final library concentration of ~30 nM in 20 μl. Libraries were amplified for a total of 10–13 cycles and were subjected to high-throughput sequencing using the Illumina HiSeq 2500 Sequencer (single end). ATAC-seq data was aligned to the genome using the same pipeline as ChIP-seq data. Data for ATAC-seq experiments are from four independent experiments with different blood donors.

ChIP and ChIP sequencing—Cells were crosslinked for 5 min at room temperature by the addition of one tenth of the volume of 11% formaldehyde solution (11% formaldehyde, 50 mM HEPES, pH 7.5, 100 mM NaCl, 1 mM EDTA, pH 8.0, and 0.5 mM EGTA, pH 8.0) to the growth medium, followed by 5 min of quenching with 100 mM glycine. Cells were pelleted at 4 °C and washed with ice-cold PBS. The crosslinked cells were lysed with lysis buffer (50 mM HEPES-KOH, pH 7.5, 140 mM NaCl, 1 mM EDTA, 10% glycerol, 0.5% NP-40 and 0.25% Triton X-100) with protease inhibitors on ice for 10 min and were washed with washing buffer (10 mM Tris-HCl, pH 8.0, 200 mM NaCl, 1 mM EDTA and 0.5 mM EGTA) for 10 min. The lysis samples were resuspended and sonicated in sonication buffer (10 mM Tris-HCl, pH 8.0, 100 mM NaCl, 1 mM EDTA, 0.5 mM EGTA, 0.1% sodium deoxycholate and 0.5% N-lauroylsarcosine) using a Bioruptor (Diagenode) with 30 s on and 30 s off on a high power output for 6 cycles. After sonication, samples were centrifuged at 12,000 r.p.m. for 10 min at 4 °C, and 1% of sonicat ed cell extracts was saved as input. The resulting whole-cell extract was incubated with Protein A Agarose for ChIP for 1 h at 4 °C. Precleared extracts were then incubated with 50 μl (50% v/v) of Protein A Agarose beads for ChIP with 5–10 μg of the appropriate antibody (listed on key resource table) overnight at 4°C. After overnight incubation, antibody-bound agarose beads were washed twice with sonication buffer, once with sonication buffer with 500 mM NaCl, once with LiCl wash buffer (10 mM Tris-HCl, pH 8.0, 1 mM EDTA, 250 mM LiCl and 1% NP-40) and once with TE with 50 mM NaCl. After washing, DNA was eluted in freshly prepared elution buffer (1% SDS and 0.1 M $NaHCO_3$). Cross-links were reversed by overnight incubation at 65 °C. RNA and protein were digested using RNase A and proteinase K, respectively, and DNA was purified with ChIP DNA Clean & Concentrator kit. For ChIP-qPCR assays, immunoprecipitated DNA was analyzed by quantitative real-time PCR and results were normalized relative to the amount of input DNA. The primer sequences for the qPCR reactions are listed in the key resource table.

For histone mark ChIP-seq experiments, 10 ng of purified immunoprecipitated DNA per sample was ligated with adaptors, and 100–300 bp DNA fragments were purified to prepare DNA libraries using a Illumina TruSeq ChIP Library Prep Kit following the manufacturer's instructions. ChIP libraries were sequenced (50 bp single end reads) using an Illumina HiSeq 2500 Sequencer at the Weill Cornell Medicine Epigenomic Core Facility per the manufacturer's recommended protocol. For input DNA to be used as control for background noise, we fragmented 1 ng of chromatin for each sample, which underwent all steps of the ChIP-seq protocol except for immunoprecipitation and washing. Then, sequenced reads

were aligned to reference human genome (GRCh37/hg19 assembly) using Bowtie2 version 2.2.6 (Langmead and Salzberg, 2012) with default parameters, and clonal reads were removed from further analysis. A minimum of 10 million uniquely mapped reads were obtained for each condition. ChIP-seq data for H2Bub, H3K4me3, H3K27ac, H4ac were previously reported and deposited in GEO GSE100383; the accession number for the H3K4me1, H3K36me3, H3K79me2, H3K56ac data is GSE129229.

For FLAG-tagged SREBP2 ChIP-seq experiments, libraries were prepared using NEBNext ultra II DNA Library prep kit from Illumina with the input amount between 2 and 10 ng. Prior to library preparation reaction, DNA was re-sheared using a Covaris E220 Evolution focused-ultrasonicator with a setting of 7°C, water level 6, 200 bp as the target peak, 175W as the peak incident power, 10% duty factor, 200 cycles per burst, 120 seconds treatment time. Library preparation was performed per manufacturer's instructions and NEBNext Multiplex oligos from Illumina were utilized for the enrichment step. The final libraries were sequenced on a Hiseq4000 (Illumina) using single-stranded 50 bp cycles. Each condition was obtained in two independent experiments from different blood donors.

Adenoviral transduction—Recombinant replication-deficient adenovirus type 5 encoding a mature form of human SREBP2 (N-SREBP2), tagged with FLAG protein (Ad-CMV-2xFLAG-SREBP2) was custom ordered from Vector Biolabs with the recombinant DNA (pcDNA3.1–2xFLAG-SREBP-2) construct purchased from Addgene (Toth et al., 2004). Control adenoviral particles encoding eGFP were obtained from Vector Biolabs. For adenoviral transduction, human monocytes were incubated for 4 days on 6-well plates at a density of 2×10^6 cells per ml in complete RPMI 1640 medium supplemented with human M-CSF (40 ng/ml). Then, the culture media was changed to low-serum media (2% FBS), followed by incubation with adenoviral particles (50 MOI) in 0.8 ml low-serum RPMI 1640 medium supplemented with human M-CSF (40 ng/ml). The plates were centrifuged at 1600 rpm at room temperature for 30 minutes. After 16 hours of transduction, the culture volume was adjusted to 3 ml with complete RPMI medium containing 10% FBS. Transduction efficiency was monitored by the fluorescence of green fluorescent protein and was typically greater than 85%.

RNA interference—For RNA interference (RNAi) experiments, primary human monocytes (10×10^6 cells) were transfected with 0.2–0.4 nmol of siRNA oligonucleotides (listed in the key resource table) using a Nucleofector kit. Human Monocyte Nucleofector buffer and the AMAXA Nucleofector System (Lonza) program Y001 for human monocytes were used according to the manufacturer's instructions.

Chitin and zymosan administration—Chitin was washed three times in PBS and then sonicated for 10 cycles (30 sec on/30 sec off) at 4°C. After filtration with a 100μm cell strainer, chitin was diluted in 50 ml PBS. About 1600 ng chitin was intraperitoneally injected, and peritoneal exudate cells (PECs) were collected 2 days after administration by flushing the peritoneal cavity with 5 mL cold PBS twice. For zymosan-elicited peritoneal macrophages, zymosan was diluted in PBS, sonicated for 10 cycles, and filtered with a 100μm cell strainer. Approximately 50μg zymosan was intraperitoneally injected and PECs were collected 1 day after injection.

Skin wound healing—Full-thickness wounds were created by excision of 4-mm punches on either side of midline (Chia et al., 2016). Prior to the surgery, aged-matched, randomly assigned mice were anesthetized with isoflurane and subcutaneous injections of buprenorphine (0.5mg/kg) were given as analgesics. Wound areas were measured by tracing onto a glass slide at the indicated time points. Slides were scanned and area calculated with ImageJ. Time-lapse photographs of the wound were taken at the indicated time points and a 2 cm marker was used in all of the photographs as a point of reference. At the indicated time points, mice were euthanized, dorsal skin was removed, and wound tissues were collected with 8-mm biopsy punches. Mice that developed anagen within 8 days after the surgery were excluded from the analyses.

Ointment for wound healing experiments—Vehicle ointment was prepared by mixing 1:1 ratio (w/w) of vaseline (Sigma) and sunflower oil (Sigma) under sterile conditions. To produce SREBP inhibitor medication ointment, betulin powder was added to the vehicle ointment with a weight ratio of 1:9. To mix the powder into the ointment, T25 digital disperser (IKA) was used at 12,000 rpm until ointment uniformity was achieved. To produce ointment for lipid synthesis inhibitors, Cerulenin (1% w/v), Atorvastatin (1%), and Hymeglusin (1%) were dissolved in sunflower oil (vehicle). Either vehicle or medication ointment was applied directly to the wound with a disposable Calcium Alginate Tipped Applicator (Puritan Medical Products Co LLC).

Histology and immunohistochemistry analysis—For murine histology, skin was fixed in Z-Fix overnight, then dehydrated in 70–100% ethanol and embedded in paraffin. Seven-micrometer sections were cut, rehydrated, and stained with H&E (Bioscientific Specialty Products, Inc).

For visualization of CD31 by immunohistochemistry, paraffin-embedded 7-μm sections were rehydrated before heat-induced antigen retrieval in EDTA, pH 9.0, for 20 minutes and then incubated with anti-CD31 antibody (1:250) for 15 minutes at room temperature. Detection of anti-CD31 antibody was done using a polymer detection system (DS9800, Novocastra Bond Polymer Refine Detection, Leica Biosystems). For SMA immunohistochemistry, 7-μm sections were rehydrated before heat-induced antigen retrieval in 10mM citrate buffer, pH 6 for 40 minutes. After antigen retrieval, anti-SMA antibody (1:300) was added for 15 minutes at room temperature to the slides. Both immunohistochemical procedures were performed on Leica Bond RX automated staining platform (Leica Biosystems).

Skin histopathology scoring—A blinded pathologist scored H&E stained sections based on the degree of wound epithelialization (0–3) at the center of the wound. Score of 0 indicates no epithelialization, while a score of 1 indicates the initial formation of hyperproliferative epithelium tongue. A score of 2 denotes complete epithelialization, but with a thin new epithelial layer (less than 4 cells deep), whereas a score of 3 marked complete and thick (>4 cell layer) epithelialization of the wound.

Flow cytometric staining, sorting, and counting—To generate single-cell suspensions of skin for flow cytometry, we adapted a previously published protocol (Chia et

al., 2016). Dorsal skin was removed, and 8-mm biopsy punches were obtained from the wounded region. Skin was finely minced before digestion in Liberase TM (13 U/ml) and then dispase II (2.42 U/ml), and then cells were isolated and used for flow cytometry (Chia et al., 2016). Anti CD16/CD32 antibodies were added to the cells for 15 minutes on ice to prevent non-specific binding of subsequent antibodies (Fc block). After Fc blocking, cells were washed and stained with CD45, F4/80 and CD11b antibodies (1:100). Stained cells were sorted on a BD Influx instrument and DAPI staining (Thermo Fisher) was performed prior to the sorting procedure to enable exclusion of dead cells. Cell quantitation was tabulated based on the number of sorted cells divided by the number of biopsy wounds in a given mouse.

Single-cell RNA sequencing—Live flow-sorted cells (DAPI negative) were prepared for single-cell sequencing at Weill Cornell Medicine Genomic Core Facility, using the SureCell WTA 3′ Library Prep Kit for the ddSeq System (Bio-Rad). DP and SP cells samples were processed from a total of eight sample chambers from two cartridges onto the Bio-Rad ddSeq Single-Cell Isolator (Bio-Rad). After completion of cDNA synthesis, cDNA from two chambers was combined into a single reaction before tagmentation, resulting in generation of four indexed libraries. Pooled libraries were sequenced on the NextSeq 500 System (Illumina) at ~150,000 reads/cell and down sampled to different read depths where indicated. Sequencing data were analyzed using the SureCell RNA Single-Cell App in BaseSpace Sequence Hub (Illumina), downsampled to ~70,000 reads. Knee plots were used to identify individual cells statistically and filter out empty beads based on unique molecular identifier (UMI) counts per cell barcode.

RNA-seq Analysis—Read quality was assessed with FastQC v0.11.6 and adapters trimmed using Cutadapt v1.15. Reads were then mapped to the human genome (hg38) and reads in exons were counted against Gencode v27 with STAR Aligner (Dobin et al., 2013). Differential gene expression analysis was performed in R using edgeR (Robinson et al., 2010). CPMs were generated in edgeR and genes with low expression levels (< 3 cpm) were filtered from all downstream analyses. Benjamini-Hochberg false discovery rate (FDR) procedure was used to correct for multiple testing. Significantly up- and down-regulated genes by TNF were defined as expressed genes with p-value < 0.01 or 0.05 and fold-change of at least 2. The RNA-seq experiments analyzed in Figures 1 and 2 were performed using three biological replicates, and in Figure 4 two biological replicates with different donors. In the three complementary experiments in Figure S3 examining the effects of cholesterol pathway inhibitors, each inhibitor compound was tested in one experiment with different donors. In these experiments, reads per kilobase transcriptome per million mapped reads (RPKM) quantification was performed using the RefSeq annotation and CuffDiff2 (Trapnell et al., 2013).

The Ingenuity Pathway Analysis (IPA)—IPA was used to analyze differently expressed genes. The Upstream Regulator analytic was used to predict upstream regulators whose change in expression or function could explain the observed gene expression changes. A z-score of higher absolute value suggests the majority of target genes for that upstream regulator were altered in a direction consistent with either inhibition or activation of the

upstream regulator, for which a negative or positive value represents the predicted inhibition or activation of the upstream regulator, respectively.

ChIP-seq and ATAC-seq Analysis—We used the *makeTagDirectory* followed by *findPeaks* command from HOMER version 4.7.2 (Heinz et al., 2010) to identify peaks of ChIP-seq enrichment over background. A false discovery rate (FDR) threshold of 0.001 was used for all datasets. The total number of mapped reads in each sample was normalized to ten million mapped reads. ChIP-seq and ATAC-seq data were visualized by preparing custom tracks for the UCSC Genome browser. For distribution plot of ChIP-seq and ATAC-seq Signals, we used the *annotatePeaks.pl* command to generate histograms for the average distribution of normalized tag densities. For de novo motif analysis, transcription factor motif finding was performed with motif finder program *findMotifsGenome.pl –size given* on the ATAC-seq peak. Peak sequences were compared to random genomic fragments of the same size and normalized G+C content to identify motifs enriched in the targeted sequences.

Functional Annotations using GREAT—GO Biological Process, MSigDB, BioCyc Pathways were compiled from GREAT version 3.0.0 (McLean et al., 2010). Pathways were ranked based on p values. The Genome Regions Enrichment of Annotations Tool (GREAT) robustly integrates distal binding events on open chromatin regions and histone marks to nearby genes to score for enrichment of various gene ontology pathways.

Single cell RNA-seq Analysis—Single cell RNA-seq analysis was performed using Seurat (Butler et al., 2018), an R package for single-cell analysis. After QC and selection of cells from the dataset using *CreateSeuratObject* command, we performed a global-scaling normalization method “LogNormalize” that normalizes the gene expression measurements for each cell by the total expression, multiplies this by a scale factor, and log-transforms the result. Then, Seurat (*FindVariableGenes* command) calculated highly variable genes across the single cells and found ~2,000 variable genes. After scaling the data and removing technical sources of variation, we performed PCA on the scaled data with the JackStraw procedure. As input to the tSNE plot, we used the same PCs as input to the clustering analysis.

QUANTIFICATION AND STATISTICAL ANALYSES

Graphpad Prism 7 for Windows was used for all statistical analysis. Detailed information about statistical analysis, including tests and values used, and number of times experiments were repeated is provided in the figure legends. *P* values are provided in the text or the figure legends. Shapiro-Wilk normality tests were performed and for data that fell within Gaussian distribution, we performed appropriate parametric statistical tests and for those that did not fall within equal variance-Gaussian distribution, we performed appropriate non-parametric statistical tests.

DATA AND SOFTWARE AVAILABILITY

The data sets that support the findings of this study and were generated by the authors as part of this study have been deposited in the Gene Expression Omnibus database with the accession code GSE129229.

Supplementary Material

Refer to Web version on PubMed Central for supplementary material.

ACKNOWLEDGEMENTS

We thank Orla O'Shea for tissue sectioning and histology, Weill Cornell Medicine Epigenomics and Genomics Core Facilities for next generation sequencing, and Weill Cornell Medicine - HSS Flow Cytometry Core Facility for cell sorting. This work was supported by grants from the N.I.H. (L.I.B., K-H.P.-M., and T.L.), the Scleroderma Foundation (T.L.), the St. Giles Foundation (T.L.), and by support for the Rosensweig Genomics Center from The Tow Foundation.

REFERENCES

Aggarwal BB (2003). Signalling pathways of the TNF superfamily: a double-edged sword. Nat Rev Immunol 3, 745–756. [PubMed: 12949498]

Akula MK, Shi M, Jiang Z, Foster CE, Miao D, Li AS, Zhang X, Gavin RM, Forde SD, Germain G, et al. (2016). Control of the innate immune response by the mevalonate pathway. Nature Immunology advance online publication

Ander BP, Dupasquier CM, Prociuk MA, and Pierce GN (2003). Polyunsaturated fatty acids and their effects on cardiovascular disease. Exp Clin Cardiol 8, 164–172. [PubMed: 19649216]

Assmann N, O'Brien KL, Donnelly RP, Dyck L, Zaiatz-Bittencourt V, Loftus RM, Heinrich P, Oefner PJ, Lynch L, Gardiner CM, et al. (2017). Srebp-controlled glucose metabolism is essential for NK cell functional responses. Nature Immunology

Bekkering S, Arts RJW, Novakovic B, Kourtzelis I, Heijden C.D.C.C.v.d., Li Y, Popa CD, Horst R.t., Tuijl J.v., Netea-Maier RT, et al. (2018). Metabolic Induction of Trained Immunity through the Mevalonate Pathway. Cell 172, 135–146.e139. [PubMed: 29328908]

Blanc M, Hsieh WY, Robertson KA, Watterson S, Shui G, Lacaze P, Khondoker M, Dickinson P, Sing G, Rodriguez-Martin S, et al. (2011). Host defense against viral infection involves interferon mediated down-regulation of sterol biosynthesis. PLoS biology 9, e1000598. [PubMed: 21408089]

Brenner D, Blaser H, and Mak TW (2015). Regulation of tumour necrosis factor signalling: live or let die. Nat Rev Immunol 15, 362–374. [PubMed: 26008591]

Brown MS, and Goldstein JL (1997). The SREBP Pathway: Regulation of Cholesterol Metabolism by Proteolysis of a Membrane-Bound Transcription Factor. Cell 89, 331–340. [PubMed: 9150132]

Butler A, Hoffman P, Smibert P, Papalexi E, and Satija R (2018). Integrating single-cell transcriptomic data across different conditions, technologies, and species. Nat Biotechnol 36, 411–420. [PubMed: 29608179]

Chen F, Liu Z, Wu W, Rozo C, Bowdridge S, Millman A, Rooijen NV, Jr JFU, Wynn TA, and Gause WC (2012). An essential role for TH2-type responses in limiting acute tissue damage during experimental helminth infection. Nature Medicine 18, 260–266.

Chia JJ, Zhu T, Chyou S, Dasoveanu DC, Carballo C, Tian S, Magro CM, Rodeo S, Spiera RF, Ruddle NH, et al. (2016). Dendritic cells maintain dermal adipose-derived stromal cells in skin fibrosis. J Clin Invest 126, 4331–4345. [PubMed: 27721238]

Dang EV, McDonald JG, Russell DW, and Cyster JG (2017). Oxysterol Restraint of Cholesterol Synthesis Prevents AIM2 Inflammasome Activation. Cell 0.

DeBose-Boyd RA, and Ye J (2018). SREBPs in Lipid Metabolism, Insulin Signaling, and Beyond. Trends Biochem Sci 43, 358–368. [PubMed: 29500098]

Dehelean CA, Soica C, Ledeti I, Aluas M, Zupko I, A, G.L., Cinta-Pinzaru S, and Munteanu M (2012). Study of the betulin enriched birch bark extracts effects on human carcinoma cells and ear inflammation. Chemistry Central journal 6, 137. [PubMed: 23158079]

Dobin A, Davis CA, Schlesinger F, Drenkow J, Zaleski C, Jha S, Batut P, Chaisson M, and Gingeras TR (2013). STAR: ultrafast universal RNA-seq aligner. Bioinformatics 29, 15–21. [PubMed: 23104886]

Eming SA, Krieg T, and Davidson JM (2007). Inflammation in wound repair: molecular and cellular mechanisms. J Invest Dermatol 127, 514–525. [PubMed: 17299434]

Eming SA, Martin P, and Tomic-Canic M (2014). Wound repair and regeneration: mechanisms, signaling, and translation. Sci Transl Med 6, 265sr266.

Eming SA, Wynn TA, and Martin P (2017). Inflammation and metabolism in tissue repair and regeneration. Science 356, 1026–1030. [PubMed: 28596335]

Fessler MB (2016). The Intracellular Cholesterol Landscape: Dynamic Integrator of the Immune Response. Trends Immunol 37, 819–830. [PubMed: 27692616]

Firestein GS, and McInnes IB (2017). Immunopathogenesis of Rheumatoid Arthritis. Immunity 46, 183–196. [PubMed: 28228278]

Folch J, Lees M, and Sloane Stanley GH (1957). A simple method for the isolation and purification of total lipides from animal tissues. J Biol Chem 226, 497–509. [PubMed: 13428781]

Ginhoux F, Schultze JL, Murray PJ, Ochando J, and Biswas SK (2016). New insights into the multidimensional concept of macrophage ontogeny, activation and function. Nat Immunol 17, 34–40. [PubMed: 26681460]

Glass CK, and Natoli G (2016). Molecular control of activation and priming in macrophages. Nat Immunol 17, 26–33. [PubMed: 26681459]

Goldstein JL, and Brown MS (2015). A Century of Cholesterol and Coronaries: From Plaques to Genes to Statins. Cell 161, 161–172. [PubMed: 25815993]

Goren I, Allmann N, Yogev N, Schürmann C, Linke A, Holdener M, Waisman A, Pfeilschifter J, and Frank S (2009). A Transgenic Mouse Model of Inducible Macrophage Depletion. Am J Pathol 175, 132–147. [PubMed: 19528348]

Guo C, Chi Z, Jiang D, Xu T, Yu W, Wang Z, Chen S, Zhang L, Liu Q, Guo X, et al. (2018). Cholesterol Homeostatic Regulator SCAP-SREBP2 Integrates NLRP3 Inflammasome Activation and Cholesterol Biosynthetic Signaling in Macrophages. Immunity 49, 842–856 e847. [PubMed: 30366764]

Heinz S, Benner C, Spann N, Bertolino E, Lin YC, Laslo P, Cheng JX, Murre C, Singh H, and Glass CK (2010). Simple combinations of lineage-determining transcription factors prime cis-regulatory elements required for macrophage and B cell identities. Mol Cell 38, 576–589. [PubMed: 20513432]

Helgadottir A, Gretarsdottir S, Thorleifsson G, Hjartarson E, Sigurdsson A, Magnusdottir A, Jonasdottir A, Kristjansson H, Sulem P, Oddsson A, et al. (2016). Variants with large effects on blood lipids and the role of cholesterol and triglycerides in coronary disease. Nat Genet 48, 634–639. [PubMed: 27135400]

Horton JD, Goldstein JL, and Brown MS (2002). SREBPs: activators of the complete program of cholesterol and fatty acid synthesis in the liver. Journal of Clinical Investigation 109, 1125–1131. [PubMed: 11994399]

Hu MS, Walmsley GG, Barnes LA, Weiskopf K, Rennert RC, Duscher D, Januszyk M, Maan ZN, Hong WX, Cheung AT, et al. (2017). Delivery of monocyte lineage cells in a biomimetic scaffold enhances tissue repair. JCI insight 2.

Hu X, Chung AY, Wu I, Foldi J, Chen J, Ji JD, Tateya T, Kang YJ, Han J, Gessler M, et al. (2008). Integrated regulation of Toll-like receptor responses by Notch and interferon-gamma pathways. Immunity 29, 691–703. [PubMed: 18976936]

Huynh L, Kusnadi A, Park SH, Murata K, Park-Min K-H, and Ivashkiv LB (2016). Opposing regulation of the late phase TNF response by mTORC1-IL-10 signaling and hypoxia in human macrophages. Scientific Reports 6, 31959. [PubMed: 27558590]

Im S-S, Yousef L, Blaschitz C, Liu Janet Z., Edwards Robert A., Young Stephen G., Raffatellu M, and Osborne Timothy F. (2011). Linking Lipid Metabolism to the Innate Immune Response in Macrophages through Sterol Regulatory Element Binding Protein-1a. Cell Metab 13, 540–549. [PubMed: 21531336]

Kalliolias GD, and Ivashkiv LB (2016). TNF biology, pathogenic mechanisms and emerging therapeutic strategies. Nat Rev Rheumatol 12, 49–62. [PubMed: 26656660]

Kidani Y, Elsaesser H, Hock MB, Vergnes L, Williams KJ, Argus JP, Marbois BN, Komisopoulou E, Wilson EB, Osborne TF, et al. (2013). The sterol regulatory element binding proteins are essential

for the metabolic programming of effector T cells and adaptive immunity. Nature immunology 14, 489–499. [PubMed: 23563690]

Kim JB, Spotts GD, Halvorsen YD, Shih HM, Ellenberger T, Towle HC, and Spiegelman BM (1995). Dual DNA binding specificity of ADD1/SREBP1 controlled by a single amino acid in the basic helix-loop-helix domain. Molecular and cellular biology 15, 2582–2588. [PubMed: 7739539]

Knipper JA, Willenborg S, Brinckmann J, Bloch W, Maaß T, Wagener R, Krieg T, Sutherland T, Munitz A, Rothenberg ME, et al. (2015). Interleukin-4 Receptor α Signaling in Myeloid Cells Controls Collagen Fibril Assembly in Skin Repair. Immunity 43, 803–816. [PubMed: 26474656]

Kratochvill F, Neale G, Haverkamp JM, Van de Velde LA, Smith AM, Kawauchi D, McEvoy J, Roussel MF, Dyer MA, Qualls JE, et al. (2015). TNF Counterbalances the Emergence of M2 Tumor Macrophages. Cell Rep 12, 1902–1914. [PubMed: 26365184]

Kroner A, Greenhalgh, Andrew D, Zarruk, Juan G, Passos dos Santos R, Gaestel M, and David S (2014). TNF and Increased Intracellular Iron Alter Macrophage Polarization to a Detrimental M1 Phenotype in the Injured Spinal Cord. Neuron 83, 1098–1116. [PubMed: 25132469]

Langmead B, and Salzberg SL (2012). Fast gapped-read alignment with Bowtie 2. Nat Methods 9, 357–359. [PubMed: 22388286]

Lawrence T, and Natoli G (2011). Transcriptional regulation of macrophage polarization: enabling diversity with identity. Nat Rev Immunol 11, 750–761. [PubMed: 22025054]

Li LC, Varghese Z, Moorhead JF, Lee CT, Chen JB, and Ruan XZ (2013). Cross-talk between TLR4-MyD88-NF-κappaB and SCAP-SREBP2 pathways mediates macrophage foam cell formation. Am J Physiol Heart Circ Physiol 304, H874–884. [PubMed: 23335792]

Liang G, Yang J, Horton JD, Hammer RE, Goldstein JL, and Brown MS (2002). Diminished hepatic response to fasting/refeeding and liver X receptor agonists in mice with selective deficiency of sterol regulatory element-binding protein-1c. J Biol Chem 277, 9520–9528. [PubMed: 11782483]

Liu SY, Aliyari R, Chikere K, Li G, Marsden MD, Smith JK, Pernet O, Guo H, Nusbaum R, Zack JA, et al. (2013). Interferon-inducible cholesterol-25-hydroxylase broadly inhibits viral entry by production of 25-hydroxycholesterol. Immunity 38, 92–105. [PubMed: 23273844]

Lucas T, Waisman A, Ranjan R, Roes J, Krieg T, Müller W, Roers A, and Eming SA (2010). Differential Roles of Macrophages in Diverse Phases of Skin Repair. The Journal of Immunology 184, 3964–3977. [PubMed: 20176743]

Marshall CD, Hu MS, Leavitt T, Barnes LA, Lorenz HP, and Longaker MT (2018). Cutaneous Scarring: Basic Science, Current Treatments, and Future Directions. Advances in wound care 7, 29–45. [PubMed: 29392092]

Matsuda M, Korn BS, Hammer RE, Moon Y-A, Komuro R, Horton JD, Goldstein JL, Brown MS, and Shimomura I (2001). SREBP cleavage-activating protein (SCAP) is required for increased lipid synthesis in liver induced by cholesterol deprivation and insulin elevation. Genes Dev 15, 1206–1216. [PubMed: 11358865]

Maurano MT, Humbert R, Rynes E, Thurman RE, Haugen E, Wang H, Reynolds AP, Sandstrom R, Qu H, Brody J, et al. (2012). Systematic localization of common disease-associated variation in regulatory DNA. Science 337, 1190–1195. [PubMed: 22955828]

McLean CY, Bristor D, Hiller M, Clarke SL, Schaar BT, Lowe CB, Wenger AM, and Bejerano G (2010). GREAT improves functional interpretation of cis-regulatory regions. Nat Biotechnol 28, 495–501. [PubMed: 20436461]

Medzhitov R (2008). Origin and physiological roles of inflammation. Nature

Minutti CM, Knipper JA, Allen JE, and Zaiss DMW (2017). Tissue-specific contribution of macrophages to wound healing. Seminars in Cell & Developmental Biology 61, 3–11. [PubMed: 27521521]

Murray PJ (2017). Macrophage Polarization. Annu Rev Physiol 79, 541–566. [PubMed: 27813830]

Murray PJ, Allen JE, Biswas SK, Fisher EA, Gilroy DW, Goerdt S, Gordon S, Hamilton JA, Ivashkiv LB, Lawrence T, et al. (2014). Macrophage activation and polarization: nomenclature and experimental guidelines. Immunity 41, 14–20. [PubMed: 25035950]

Nathan C, and Ding A (2010). Nonresolving Inflammation. Cell 140, 871–882. [PubMed: 20303877]

O'Neill LAJ, Kishton RJ, and Rathmell J (2016). A guide to immunometabolism for immunologists. Nature Reviews Immunology 16, 553–565.

Oishi Y, Spann NJ, Link VM, Muse ED, Strid T, Edillor C, Kolar MJ, Matsuzaka T, Hayakawa S, Tao J, et al. (2017). SREBP1 Contributes to Resolution of Pro-inflammatory TLR4 Signaling by Reprogramming Fatty Acid Metabolism. Cell Metab

Osborne TF, and Espenshade PJ (2009). Evolutionary conservation and adaptation in the mechanism that regulates SREBP action: what a long, strange tRIP it's been. Genes Dev 23, 2578–2591. [PubMed: 19933148]

Ouyang N, Gan H, He Q, Lei H, Wang SY, Liu Q, and Zhou C (2018). Dysfunction of cholesterol sensor SCAP promotes inflammation activation in THP-1 macrophages. Exp Cell Res 367, 162–169. [PubMed: 29596892]

Park SH, Kang K, Giannopoulou E, Qiao Y, Kang K, Kim G, Park-Min K-H, and Ivashkiv LB (2017). Type I interferons and the cytokine TNF cooperatively reprogram the macrophage epigenome to promote inflammatory activation. Nature Immunology *advance online publication*.

Park SH, Park-Min K-H, Chen J, Hu X, and Ivashkiv LB (2011). Tumor necrosis factor induces GSK3 kinase-mediated cross-tolerance to endotoxin in macrophages. Nature Immunology 12, 607–615. [PubMed: 21602809]

Park YH, Wood G, Kastner DL, and Chae JJ (2016). Pyrin inflammasome activation and RhoA signaling in the autoinflammatory diseases FMF and HIDS. Nature Immunology *advance online publication*.

Perretti M, Cooper D, Dalli J, and Norling LV (2017). Immune resolution mechanisms in inflammatory arthritis. Nat Rev Rheumatol 13, 87–99. [PubMed: 28053331]

Reboldi A, Dang EV, McDonald JG, Liang G, Russell DW, and Cyster JG (2014). 25-hydroxycholesterol suppresses interleukin-1-driven inflammation downstream of type I interferon. Science 345, 679–684. [PubMed: 25104388]

Reed BD, Charos AE, Szekely AM, Weissman SM, and Snyder M (2008). Genome-wide occupancy of SREBP1 and its partners NFY and SP1 reveals novel functional roles and combinatorial regulation of distinct classes of genes. PLoS genetics 4, e1000133. [PubMed: 18654640]

Robinson MD, McCarthy DJ, and Smyth GK (2010). edgeR: a Bioconductor package for differential expression analysis of digital gene expression data. Bioinformatics 26, 139–140. [PubMed: 19910308]

Rong S, Cortes VA, Rashid S, Anderson NN, McDonald JG, Liang G, Moon YA, Hammer RE, and Horton JD (2017). Expression of SREBP-1c Requires SREBP-2-mediated Generation of a Sterol Ligand for LXR in Livers of Mice. Elife 6.

Satoh T, Takeuchi O, Vandenbon A, Yasuda K, Tanaka Y, Kumagai Y, Miyake T, Matsushita K, Okazaki T, Saitoh T, et al. (2010). The Jmjd3-Irf4 axis regulates M2 macrophage polarization and host responses against helminth infection. Nature Immunology 11, 936–944. [PubMed: 20729857]

Seo YK, Chong HK, Infante AM, Im SS, Xie X, and Osborne TF (2009). Genome-wide analysis of SREBP-1 binding in mouse liver chromatin reveals a preference for promoter proximal binding to a new motif. Proceedings of the National Academy of Sciences of the United States of America 106, 13765–13769. [PubMed: 19666523]

Seo YK, Jeon T-I, Chong HK, Beisinger J, Xie X, and Osborne TF (2011). Genome-wide Localization of SREBP-2 in Hepatic Chromatin Predicts a Role in Autophagy. Cell Metab 13, 367–375. [PubMed: 21459322]

Sharif MN, Sosic D, Rothlin CV, Kelly E, Lemke G, Olson EN, and Ivashkiv LB (2006). Twist mediates suppression of inflammation by type I IFNs and Axl. The Journal of experimental medicine 203, 1891–1901. [PubMed: 16831897]

Shimano H, Shimomura I, Hammer RE, Herz J, Goldstein JL, Brown MS, and Horton JD (1997). Elevated levels of SREBP-2 and cholesterol synthesis in livers of mice homozygous for a targeted disruption of the SREBP-1 gene. J Clin Invest 100, 2115–2124. [PubMed: 9329978]

Sindrilaru A, Peters T, Wieschalka S, Baican C, Baican A, Peter H, Hainzl A, Schatz S, Qi Y, Schlecht A, et al. (2011). An unrestrained proinflammatory M1 macrophage population induced by iron impairs wound healing in humans and mice. J Clin Invest 121, 985–997. [PubMed: 21317534]

Sosic D, Richardson JA, Yu K, Ornitz DM, and Olson EN (2003). Twist regulates cytokine gene expression through a negative feedback loop that represses NF-κappaB activity. Cell 112, 169–180. [PubMed: 12553906]

Soyal SM, Nofziger C, Dossena S, Paulmichl M, and Patsch W (2015). Targeting SREBPs for treatment of the metabolic syndrome. Trends in Pharmacological Sciences 36, 406–416. [PubMed: 26005080]

Spann NJ, Garmire LX, McDonald JG, Myers DS, Milne SB, Shibata N, Reichart D, Fox JN, Shaked I, Heudobler D, et al. (2012). Regulated accumulation of desmosterol integrates macrophage lipid metabolism and inflammatory responses. Cell 151, 138–152. [PubMed: 23021221]

Streit M, Beleznay Z, and Braathen LR (2006). Topical application of the tumour necrosis factor-α antibody infliximab improves healing of chronic wounds. International Wound Journal 3, 171–179. [PubMed: 16984574]

Tabas I, and Lichtman AH (2017). Monocyte-Macrophages and T Cells in Atherosclerosis. Immunity 47, 621–634. [PubMed: 29045897]

Tall AR, and Yvan-Charvet L (2015). Cholesterol, inflammation and innate immunity. Nature Reviews Immunology 15, 104–116.

Teich N, and Klugmann T (2014). Rapid improvement of refractory pyoderma gangrenosum with infliximab gel in a patient with ulcerative colitis. J Crohns Colitis 8, 85–86. [PubMed: 23810275]

Tong A-J, Liu X, Thomas BJ, Lissner MM, Baker MR, Senagolage MD, Allred AL, Barish GD, and Smale ST (2016). A Stringent Systems Approach Uncovers Gene-Specific Mechanisms Regulating Inflammation. Cell 165, 165–179. [PubMed: 26924576]

Toth JI, Datta S, Athanikar JN, Freedman LP, and Osborne TF (2004). Selective coactivator interactions in gene activation by SREBP-1a and −1c. Molecular and cellular biology 24, 8288–8300. [PubMed: 15340088]

Trapnell C, Hendrickson DG, Sauvageau M, Goff L, Rinn JL, and Pachter L (2013). Differential analysis of gene regulation at transcript resolution with RNA-seq. Nat Biotechnol 31, 46–53. [PubMed: 23222703]

Wei W, Schwaid AG, Wang X, Wang X, Chen S, Chu Q, Saghatelian A, and Wan Y (2016). Ligand Activation of ERRalpha by Cholesterol Mediates Statin and Bisphosphonate Effects. Cell Metab 23, 479–491. [PubMed: 26777690]

Wynn TA, and Vannella KM (2016). Macrophages in Tissue Repair, Regeneration, and Fibrosis. Immunity 44, 450–462. [PubMed: 26982353]

Yarilina A, Park-Min K-H, Antoniv T, Hu X, and Ivashkiv LB (2008). TNF activates an IRF1-dependent autocrine loop leading to sustained expression of chemokines and STAT1-dependent type I interferon–response genes. Nature Immunology 9, 378–387. [PubMed: 18345002]

York Autumn G., Williams Kevin J., Argus Joseph P., Zhou Quan D., Brar G, Vergnes L, Gray Elizabeth E., Zhen A, Wu Nicholas C., Yamada Douglas H., et al. (2015). Limiting Cholesterol Biosynthetic Flux Spontaneously Engages Type I IFN Signaling. Cell 163, 1716–1729. [PubMed: 26686653]

Zhao R, Liang H, Clarke E, Jackson C, and Xue M (2016). Inflammation in Chronic Wounds. Int J Mol Sci 17.

Highlights

- TNF induces late phase activation of SREBP2 and cholesterol genes in macrophages
- SREBP2 binds and activates inflammatory target genes in TNF-stimulated macrophages
- Inhibition of the TNF-SREBP axis promotes M2-like polarization and wound healing
- The TNF-SREBP axis is an attractive therapeutic target for promoting tissue repair

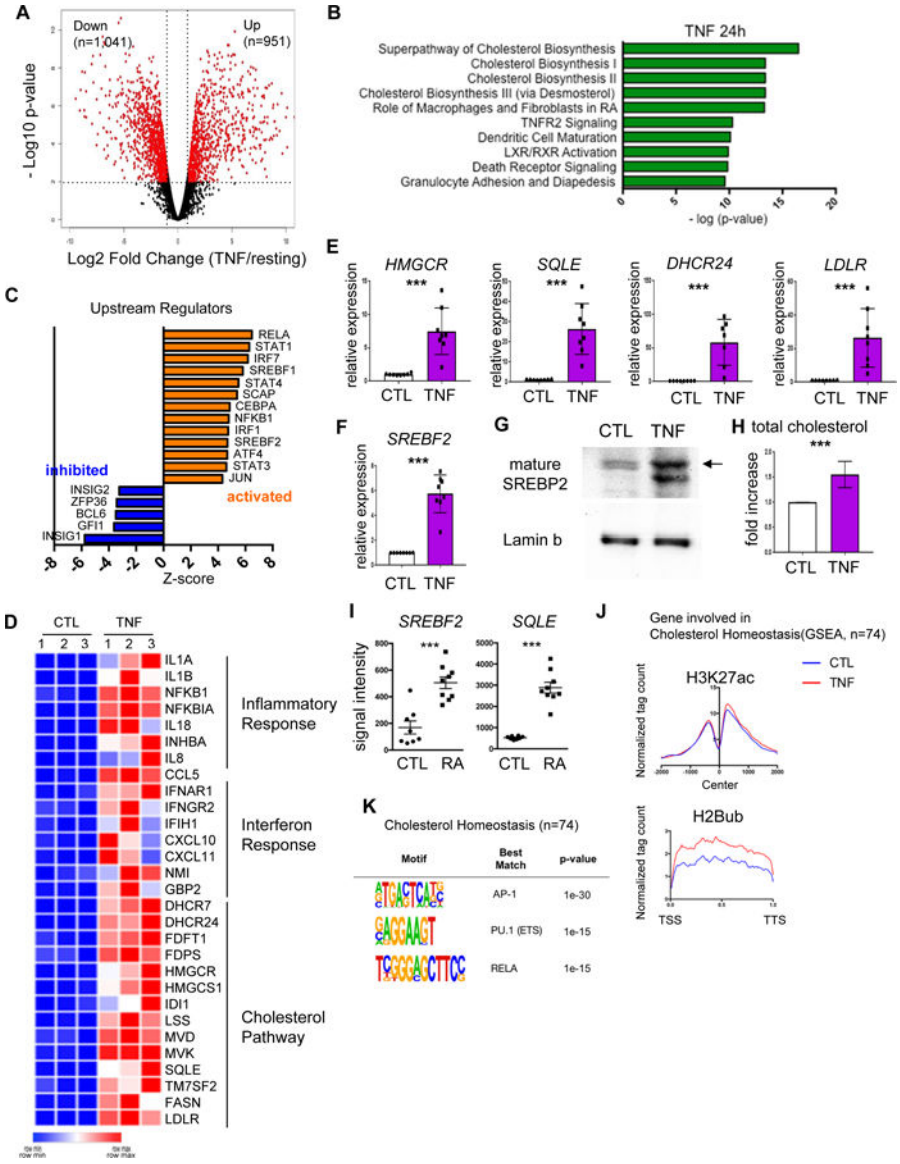

Figure 1. Cholesterol synthesis pathway and its regulator SREBP2 are activated in the late phase TNF response

Primary human monocytes were treated with or without TNF (10 ng/ml) for 16–24 hours.

(A) Volcano plot of RNAseq analysis of differentially expressed genes. Red dots show genes with significant ($p<0.01$) and greater than 2-fold changes.

(B and C) Ingenuity Pathway Analysis of TNF-inducible genes from (A).

(D) Heatmap of representative TNF-inducible genes from (A) showing 3 independent donors.

(E and F) qPCR analysis of mRNA amounts normalized relative to *TBP* (n = 8). Data are represented as mean ± SD.

(G) Immunoblot of SREBP2 protein (arrow) in nuclear lysates. Arrow marks SREBP2 band that comigrated with SREBP2 in positive control lysates. Lamin B serves as a normalization control. (n = 3)

(H) Quantitation of total cholesterol in cells treated without or with TNF (n = 8).

(I) Gene expression in control (n=8) and RA synovial fluid (n=9) macrophages. Based on microarray data in GEO GSE97779.
(J) Normalized H3K27ac and H2Bub tag density at genes (n=74) involved in cholesterol homeostasis.
(K) *De novo* motif analysis of DNA sequences enriched under TNF-inducible ATAC-seq peaks associated with genes in the cholesterol pathway.
**p<0.01; ***p<0.001; ****p<0.0001 by Mann-Whitney test (E, F, H) and paired Student t-test (I). Data represent analysis of three independent experiments with different blood donors (A-C), 8 independent experiments (E, F, H), or are representative of two (J) or three (G, K) experiments.
See also Figures S1 and S2.

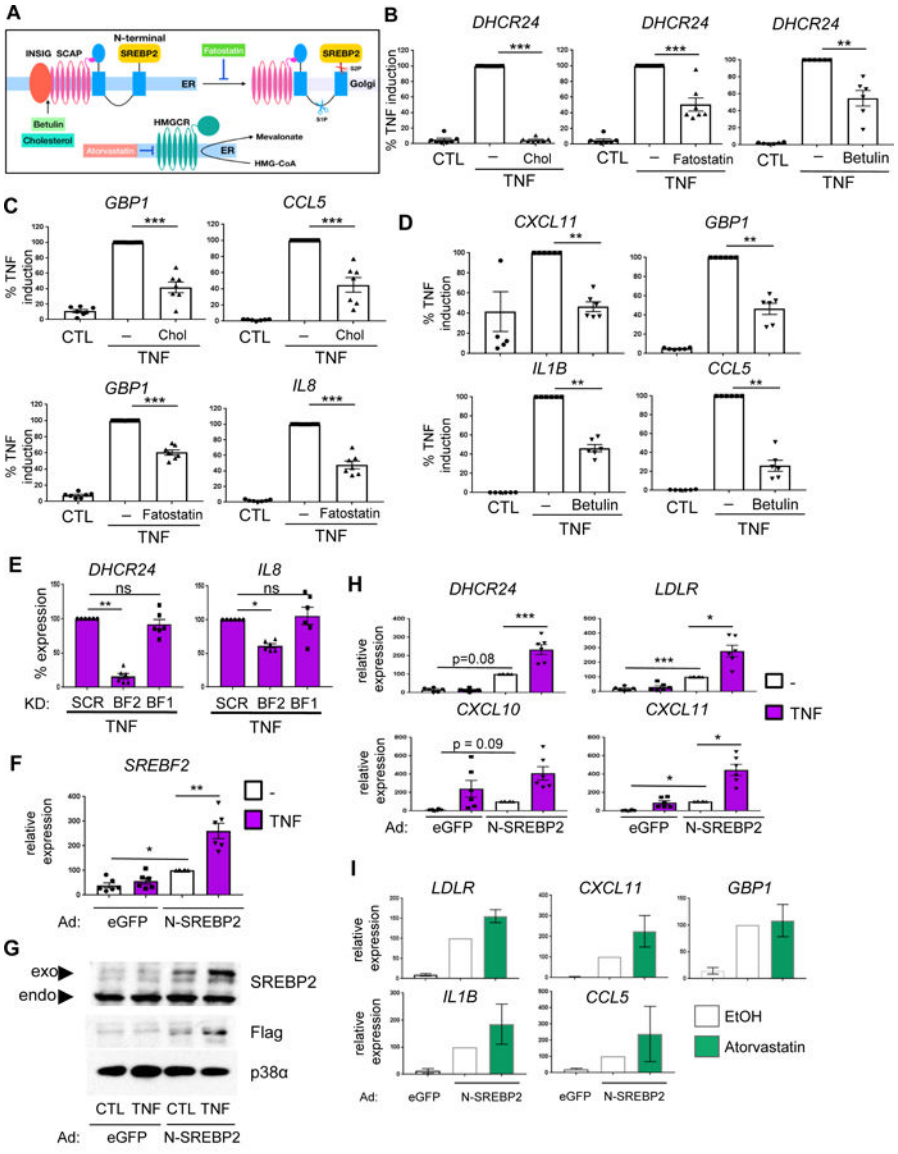

Figure 2. SREBP2 promotes late phase TNF-induced inflammatory phenotype independently of cholesterol

(A) Schematic depicting site of action of four different inhibitors of SREBP and cholesterol synthesis.

(B-D) RT-qPCR analysis of gene expression in macrophages stimulated with TNF with vehicle control or cholesterol:MCD (10μg/ml), fatostatin (20μM), or betulin (3μg/ml).

(E) RT-qPCR analysis of mRNA from human macrophages transfected with scrambled control (SCR), *SREBF1*-specific (BF1), or *SREBF2*-specific (BF2) siRNAs.

(F, H) RT-qPCR analysis of mRNA in human macrophages transduced with adenoviral particles encoding eGFP or FLAG-N-SREBP2.

(G) Immunoblot of whole cell lysates from human macrophages transduced with adenoviral particles encoding eGFP or FLAG-N-SREBP2 probed with SREBP2 or FLAG antibodies. Endo = endogenous SREBP2, exo = exogenous SREBP2 which migrates at a larger molecular mass because of FLAG tag. p38α serves as a loading control.

(I) RT-qPCR analysis of RNA from human macrophages transduced with adenoviral particles encoding eGFP or FLAG-N-SREBP2 and stimulated with TNF in the absence or presence of atorvastatin (10μM). (n=3)

In (B-F), (H) and (I) data are normalized relative to *TBP* and presented as mean ± SEM. Each dot represents one biological replicate and data are shown normalized to the TNF-stimulated condition, which is set at 100. *p<0.05; **p<0.01; ***p<0.001; ****p<0.0001 by Friedman test (E), Mann-Whitney test (B,C,D,I), and Kruskal-Wallis test (F, H). Data represent three (I), six (D, E, F, H) or seven (B, C) independent experiments with different donors.

See also Figure S3.

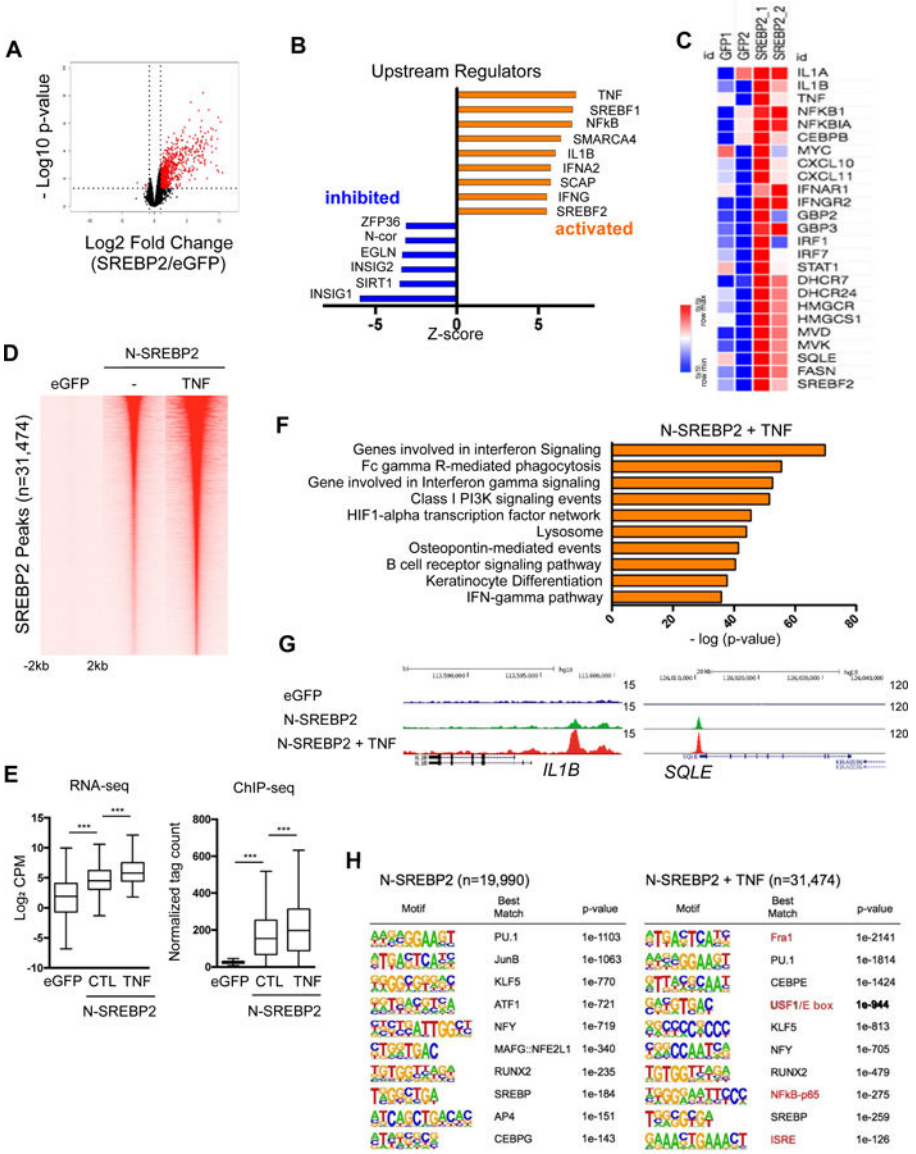

Figure 3. SREBP2 binds to late phase TNF-induced interferon and inflammatory response gene loci

(A) Volcano plot of RNAseq analysis of human macrophages transduced with adenoviral particles encoding eGFP or FLAG-N-SREBP2. Colored dots correspond to genes with significant ($p < 0.05$) and greater than two-fold expression changes.

(B) Ingenuity Pathway Analysis of upstream regulators of genes whose expression was significantly induced by N-SREBP2 in (A).

(C) Heatmap of representative genes induced by N-SREBP2 in (A).

(D) ChIP-seq analysis of SREBP2 in human macrophages transduced with adenoviral particles encoding eGFP or FLAG-N-SREBP2 and immunoprecipitated with FLAG antibodies. Data are presented as normalized tag density ± 2kb around peak centers.

(E) Boxplots showing normalized tag counts of SREBP2 peaks (right) associated with SREBP2-induced genes (left panel).

(F) MSigDB pathways showing significant enrichment of SREBP2-associated genes.

(G) Representative UCSC genome browser tracks.

(H) *De novo* motif-enrichment analysis under SREBP2 peaks; random background regions serve as a control.

Data (A-H) is representative of two independent experiments with different blood donors. See also Figure S4 and S5.

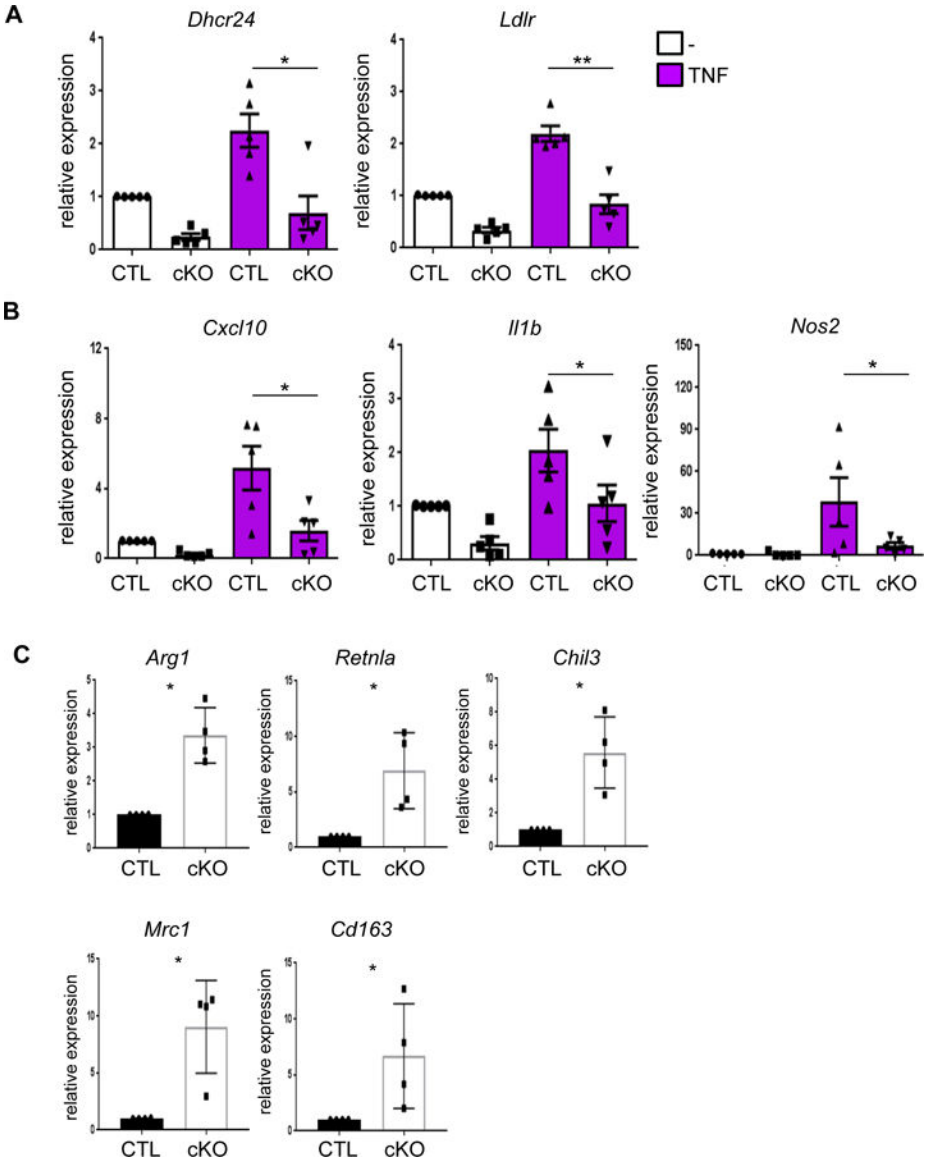

Figure 4. SREBP inactivation in murine macrophages shifts TNF-induced polarization from inflammatory towards reparative

(A-B) RT-qPCR analysis of mRNA from zymosan-elicited peritoneal macrophages from control or *Scap*-deficient mice (cKO) stimulated *ex vivo* with TNF (40 ng/ml) for 8 hr (mean ± SEM).

(C) RT-qPCR analysis of mRNA from freshly isolated control and *Scap*-deficient chitin elicited-peritoneal macrophages (mean ± SD).

Data are normalized relative to *Tbp*. Each dot represents one mouse and data represent results from five (A, B) or four (C) mice in at least three independent experiments. *p<0.05; **p<0.01; ***p<0.001; ****p<0.0001 by Mann-Whitney test (A, C) or paired Student t-test (B).

See also Figure S5.

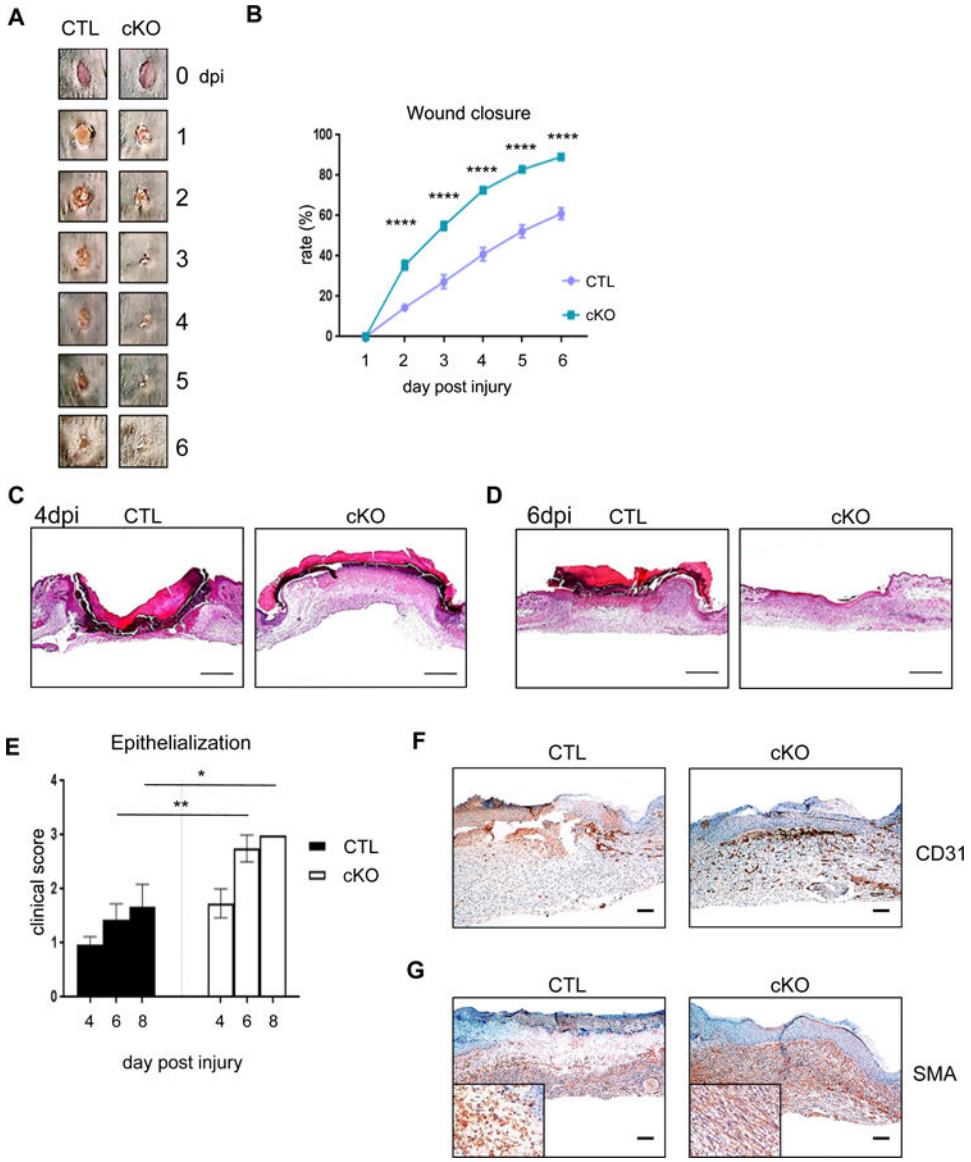

Figure 5. Myeloid-SREBP activity suppresses epidermal and dermal healing

(A) Representative time-lapse photographs of skin wounds in control and myeloid *Scap*-deficient mice over 6 dpi.

(B) Wound area in control and myeloid *Scap*-deficient mice over 6 dpi (n = 14 wounds of 7 mice per genotype).

(C) Representative H&E images of 4 dpi wounds from control (n = 6) and myeloid *Scap*-deficient (n = 7) mice.

(D) Representative H&E images of 6 dpi wounds (n = 7–8 per genotype).

(E) Histological scores of wound epithelialization (n = 6–8 wounds of 6–8 mice per genotype).

(F, G) Representative immunohistochemical staining for CD31 (F) and SMA (G) at 6 dpi (n = 6 per genotype).

Data are generated from at least 3 independent experiments per time point. The scale bar represents 100μm. Data are presented as mean ± SEM. *p<0.05; **p<0.01; ****p<0.0001 by two-way ANOVA. See also Figure S6.

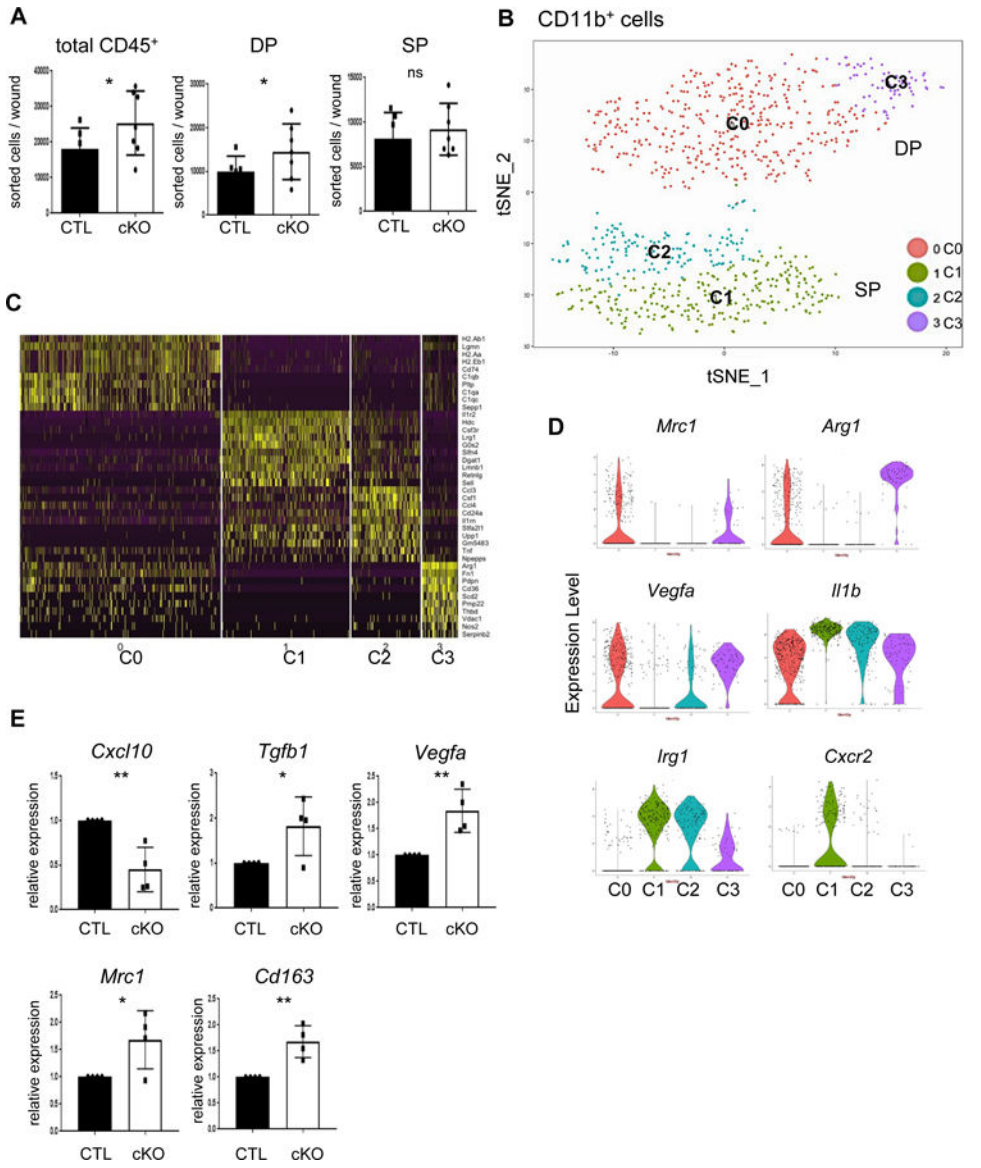

Figure 6. SREBP regulates infiltration and phenotype of wound macrophages

(A) Flow cytometric quantitation of CD45+, CD11b+ F4/80+ (DP), and CD11b+ F4/80- (SP) sorted cells in control and *Scap*-deficient mice at 4 dpi. Each dot represents one mouse (n = 7).

(B) tSNE plot of macrophages from wounds at 4 dpi. A total 857 cells are depicted as individual dots on the plot. The algorithm assigned cells into 4 different clusters, labeled C0-C3.

(C) Heatmap visualization of the 10 most highly expressed genes in each cell cluster.

(D) Violin plots of expression of representative genes in each cell cluster.

(E) RT-qPCR analysis of gene expression in DP cells from control or *Scap*-deficient mice at 6 dpi (n=4 per genotype). Data were normalized relative to *Tbp*. Each dot represents one mouse and the data are represented as mean ± SD. At least three independent experiments were performed. *p<0.05; **p<0.01 by Student t-test. See also Figure S6 and S7.

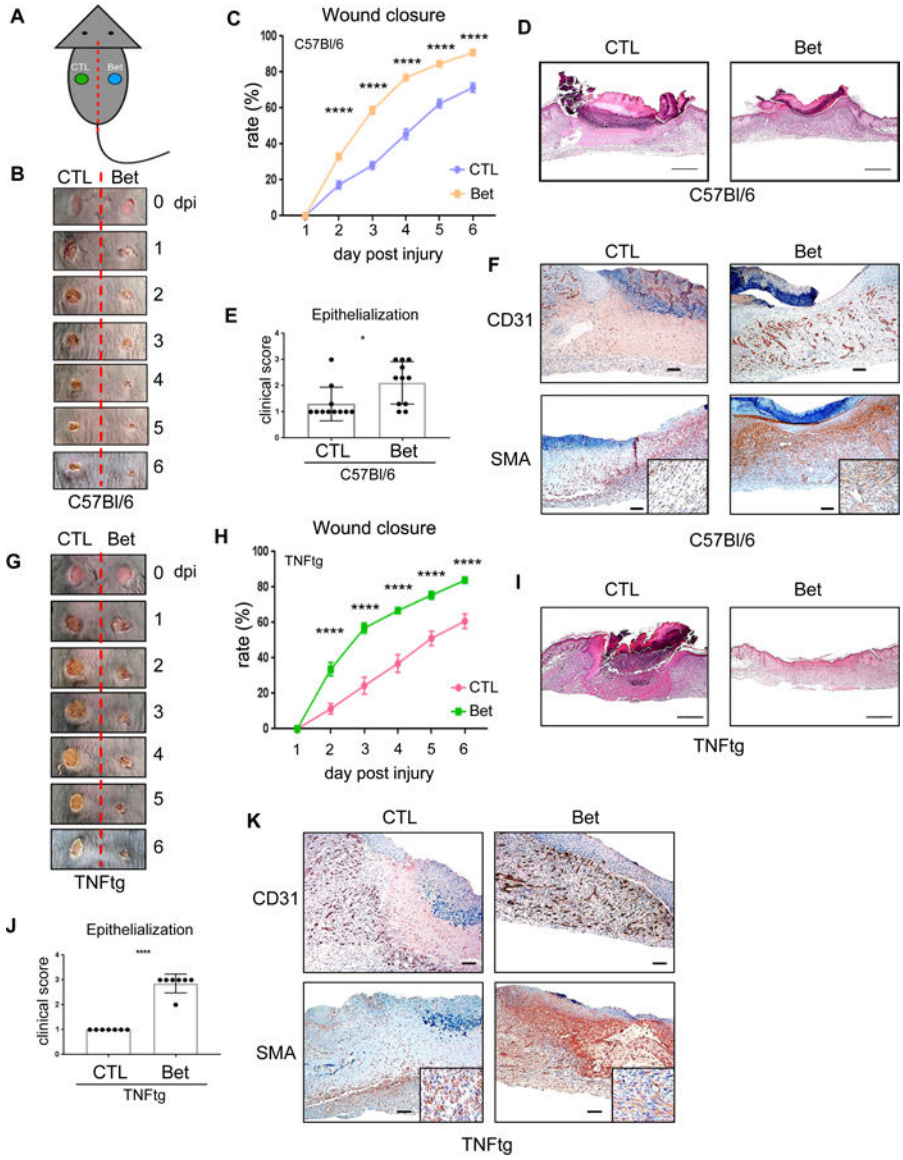

Figure 7. Topical inhibition of SREBP accelerates wound healing under homeostatic and chronic inflammatory conditions

(A) Schematic of treatment with daily application of control ointment on the sinistral side and betulin on the dextral side.

(B) Representative time-lapse photographs of skin wounds in C57BL/6 mice over 6 dpi, treated with control or betulin ointment.

(C) Wound area after control and betulin treatment of C57BL/6 mice. Two-way ANOVA.

(D) Representative H&E images of 6 dpi wounds (n = 6).

(E) Histological scores of wound epithelialization at 6 dpi for control and betulin treated wounds in C57BL/6 mice (n = 11 wounds per condition in 6 female mice; each dot represents one wound). Paired student t-test.

(F) Representative immunohistochemical staining for CD31 (upper panels) and SMA (lower panels) of wound sections at 6 dpi (n = 3).

(G) Representative time-lapse photographs of skin wounds in TNF-Tg mouse over 6 dpi, treated with control or betulin ointment.
(H) Wound area in control and betulin-treated wounds in TNF-Tg mice. Two-way ANOVA.
(I) Representative H&E images of wounds 6 dpi from TNF-Tg mice (n = 7).
(J) Histological scores of wound epithelialization at 6 dpi for control or betulin treated wounds in TNF-Tg mice (n = 7 wounds per condition in 7 female mice; each dot represents one wound). Paired Student t-test.
(K) Representative immunohistochemical staining for CD31 (upper panels) and SMA (lower panels) of wound sections in TNF-Tg mice treated with control (left) or betulin (right) ointment at 6 dpi (n = 3).
Data in (A-F) and in (G-K) are pooled from 2 independent experiments. Data are presented as mean ± SEM. The scale bars represent 100μm. *p<0.05; ****p<0.0001. See also Figure S7.

KEY RESOURCES TABLE

REAGENT or RESOURCE	SOURCE	IDENTIFIER
Antibodies		
Monoclonal mouse anti-FLAG M2 antibody	Sigma Aldrich	RRID:AB_259529
Polyclonal rabbit anti-H3K4me3 antibody	Abcam	RRID:AB_306649
Polyclonal rabbit anti-H3K4me1 antibody	Abcam	RRID:AB_306847
Polyclonal rabbit anti-H3K27ac antibody	Abcam	RRID:AB_2118291
Polyclonal rabbit anti-H3K36me3 antibody	Abcam	RRID:AB_306966
Monoclonal rabbit anti-H2Bub antibody	Cell Signaling Tech	RRID:AB_10693452
Polyclonal rabbit anti-H3K56ac antibody	Active Motif	RRID:AB_2661786
Polyclonal rabbit anti-H3K79me2 antibody	Active Motif	RRID:AB_2561018
Polyclonal rabbit anti-H4ac antibody	EMD Milipore	RRID:AB_310270
Polyclonal rabbit anti-SREBP2 antibody	Abcam	RRID:AB_779079
Polyclonal rabbit anti-Laminb1 antibody	Abcam	RRID:AB_443298
Polyclonal rabbit anti-p38alpha antibody	Santa Cruz	RRID:AB_632138
Monoclonal rat anti-CD31	Dianova	RRID:AB_2631039
Monoclonal rabbit anti-SMA antibody	Epitomics	Cat# 1184–1
APC/Cy7 rat anti-mouse CD45 antibody	Biolegend	RRID:AB_312980
Purified rat anti-mouse CD16/CD32 antibody	BD Biosciences	RRID:AB_394657
FITC rat anti-mouse F4/80 antibody	Biolegend	RRID:AB_893500
BV570 rat anti-mouse/human CD11b antibody	Biolegend	RRID:AB_10896949
PE rat anti-mouse NK1.1 antibody	Biolegend	RRID:AB_313394
AF700 rat anti-mouse B220 antibody	Biolegend	RRID:AB_493716
PE/Cy7 rat anti-mouse CD3 antibody	Biolegend	RRID:AB_1732068
APC rat anti-mouse Ly6G antibody	Biolegend	RRID:AB_1877163
PB rat anti-mouse Ly6C antibody	Biolegend	RRID:AB_1732090
CD14 microbeads, human	Miltenyi Biotec	RRID:AB_2665482
Polyclonal rabbit anti-STAT6 (phospho Y641) antibody	Abcam	RRID:AB_778116
Polyclonal rabbit anti-STAT6 (total) antibody	Cell Signaling Tech	RRID:AB_2271211
Monoclonal rabbit anti-β-Actin antibody	Cell Signaling Tech	RRID:AB_10950489
CD11b microbeads, mouse and human	Miltenyi Biotec	Cat# 130–049-601
Mouse antibody against human-IFNAR	PBL Interferon Source	RRID:AB_387828
Mouse IgG2a Isotype Control	Ancell	Cat# 281–810
Bacterial and Virus Strains		
eGFP adenovirus	Vector biolabs	Cat# 1060
CMV-2xFLAG-SREBF2 adenovirus	Vector biolabs	custom made, N/A

REAGENT or RESOURCE	SOURCE	IDENTIFIER
Biological Samples		
Human Peripheral Blood Mononuclear Cells	New York Blood Center	N/A
Chemicals, Peptides, and Recombinant Proteins		
Atorvastatin calcium salt trihydrate	Sigma Aldrich	Cat# PZ0001
SB202190	Tocris Bioscience	Cat# 1264
PD98059	Tocris Bioscience	Cat# 1213
SP600125	Tocris Bioscience	Cat# 1496
Betulin	Sigma Aldrich	Cat# B9757
Cholesterol-Water Soluble	Sigma Aldrich	Cat# C4951
Fatostatin A	Tocris Bioscience	Cat# 4444
Hymeglusin	Sigma Aldrich	Cat# SML0301
Cerulenin	Sigma Aldrich	Cat# C2389
Zymosan A	Sigma Aldrich	Cat# Z4250
Chitin	Sigma Aldrich	Cat# C7170
Thioglycollate Medium	Sigma Aldrich	Cat# T9032
Sunflower seed oil	Sigma Aldrich	Cat# S5007
Vaseline	Sigma Aldrich	Cat# 16415
RNase A	Sigma Aldrich	Cat# 11119915001
Proteinase K	Life Technologies	Cat# AM2548
Pefabloc SC	Sigma Aldrich	Cat# 76307
Buprenorphine hydrochloride	Reckitt Benckiser Healthcare Ltd.	Cat# 12496–0757-5
BODIPY 493/503	Thermo Fisher Scientific	Cat# D3922
Z-Fix	Anatech ltd	Cat# SKU:170
Dynabeads Protein A	Invitrogen	Cat# 100–02D
Human recombinant TNF	Peprotech	Cat# 300–01A
Murine recombinant TNF	Peprotech	Cat# 315–01A
Human recombinant M-CSF	Peprotech	Cat# 300–25
Human recombinant IFN-α	PBL Interferon Source	Cat# 11100–1
Human recombinant IL-4	Peprotech	Cat# 200–04
Murine recombinant IL-4	Peprotech	Cat# 214–14
Liberase TM	Sigma Aldrich	Cat# 5401127001
Dispase II	Thermo Fisher	Cat# 17105041
Lymphoprep	Stemcell Technologies	Cat# 07801
Critical Commercial Assays		
Amplex Red Cholesterol Assay kit	Life Technologies	Cat# A12216
First strand cDNA synthesis kit	Fermentas	Cat# K1622

REAGENT or RESOURCE	SOURCE	IDENTIFIER
RNeasy mini kit	Qiagen	Cat# 74104
Nucleofector kits for human monocytes	Lonza	Cat# V4XP-3032
Fast SYBR Green Master Mix	Life Technologies	Cat# 4385618
TruSeq ChIP Library Preparation kit	Illumina	Cat# IP-202–1012
NEBNext Ultra II DNA Library Prep kit for Illumina	New England Biolabs	Cat# E7645S
NEBNext Multiplex Oligos for Illumina (Index Primers Set 1)	New England Biolabs	Cat# E7335S
TruSeq RNA Library Preparation v2 kit	Illumina	Cat# RS-122–2001
ChIP DNA Clean and Concentrator	Zymo Research	Cat# D5205
MinElute PCR Purification kit	Qiagen	Cat# 28006
QIAquick PCR Purification kit	Qiagen	Cat# 28106
NEBNext High-Fidelity 2x PCR Master Mix	New England Biolabs	Cat# M0541S
NEBNext Multiplex Oligos for Illumina	New England Biolabs	Cat# E7335S
SureCell WTA 3′ Library Prep Kit for the ddSeq System	Illumina	Cat# 200142780
Deposited Data		
ChIP-seq and ATAC-seq	Park et al, 2017	GEO: GSE100383
Microarray data	Kang et al., 2017	GEO: GSE97779
RNA-seq, ChIP-seq and ATAC-seq	This Paper	GEO: GSE129229
Single cell RNA-seq	This Paper	GEO: GSE129229
Experimental Models: Organisms/Strains		
LysM Cre: B6.129P2-Lyz2tm1(cre)Ifo/J	Jackson Laboratory	RRID:IMSR_JAX:004781
Scap flox: B6;129-*Scap*^{tm1Mbjg}/J	Jackson Laboratory	RRID:IMSR_JAX:004162
C57BL/6J	Jackson Laboratory	RRID:IMSR_JAX:000664
TNF tg: B6.Cg-Tg(TNF)#Xen	Taconic farms	Cat# 1006
WT control: B6.Cg-Tg(TNF)#Xen	Taconic farms	Cat# 1006
Oligonucleotides		
qPCR human *TBP* primers: F:5’-CACCACAGCT CTTCCACTCA-3’ R:5’-GGGGAGGGATACAGTGGAGT-3’	This paper	N/A
qPCR human *HMGCR* primers: F:5’-TGATTGACCTTTCCAGAGCAAG-3’ R:5’-CTAAAATTGCCATTCCACGAGC-3’	This paper	N/A
qPCR human *SQLE* primers: F:5’-TGACAATTCTCATCTGAGGTCCA-3’ R:5’ -CAGGGATACCCTTTAGCAGTTTT-3’	This paper	N/A
qPCR human *DHCR24* primers: F:5’-GCCGCTCTCGCTTATCTTCG-3’ R:5’-GTCTTGCTACCCTGCTCCTT-3’	This paper	N/A
qPCR human *LDLR* primers: F:5’-TCTGCAACATGGCTAGAGACT-3’ R:5’-TCCAAGCATTCGTTGGTCCC-3’	This paper	N/A
qPCR human *SREBF2* primers: F:5’-AACGGTCATTCACCCAGGTC-3’ R:5’-GGCTGAAGAATAGGAGTTGCC-3’	This paper	N/A

REAGENT or RESOURCE	SOURCE	IDENTIFIER
qPCR human *CXCL10* primers: F:5'-ATTTGCTGCCTTATCTTTCTG-3' R:5'-TCTCACCCTTCTTTTTCATTGTAG-3'	This paper	N/A
qPCR human *CXCL11* primers: F:5'-GAAGGATGAAAGGTGGGTGA-3' R:5'-AAGCACTTTGTAAACTCCGATG-3'	This paper	N/A
qPCR human *GBP1* primers: F:5'-TGGAACGTGTGAAAGCTGAGTCT-3' R:5'-CATCTGCTCATTCTTTCTTTGCA-3'	This paper	N/A
qPCR human *IL1B* primers: F:5'-TTCTTCGACACATTGGATAACG-3' R:5'-TGGAGAACACCACTTGTTGCT-3'	This paper	N/A
qPCR human *CCL5* primers: F:5'-GAGGCTTCCCCTCACTATCC-3' R:5'-CTCAAGTGATCCACCCACCT-3'	This paper	N/A
qPCR human *IL8* primers: F:5'-TCTGTTAAATCTGGCAACCC-3' R:5'-TAAAGGAGAAACCAAGGCAC-3'	This paper	N/A
ChIP-qPCR human *HBB* promoter primers: F:5'-GAGGCCTCAGCGGTTTCAAGT-3' R:5'-TGCTCCTGGGAGTAGATTGG-3'	This paper	N/A
ChIP-qPCR human *DHCR24* promoter primers: F:5'-GGGAGAAAAGGGTGGAG-3' R:5'-GTTCGCGCCTCCTGTC-3'	This paper	N/A
ChIP-qPCR human *LDLR* promoter primers: F:5'-CATCGAGAAATTTCAGGAGGA-3' R:5'-AATGTGAGGTTTCTAGCAGGG-3'	This paper	N/A
ChIP-qPCR human *CXCL10* promoter primers: F:5'-CAAAACCTGCTGGCTGTTCC-3' R:5'-GGAAATTCCGTAACTTGGAGGC-3'	This paper	N/A
ChIP-qPCR human *IL1B* regulatory region primers: F:5'-CACAGCACTTCCTTCCGATC-3' R:5'-TTTCCAGCTCCCCATCTCTG-3'	This paper	N/A
ChIP-qPCR human *CCL15* promoter primers: F:5'-CATGCGGAATGCCAGCATAT-3' R:5'-GAGACAAGATTTAGAGCAGG-3'	This paper	N/A
qPCR murine *Tbp* primers: F:5'-AGAACAATCCAGACTAGCAGCA-3' R:5'-GGGAACTTCACATCACAGCTC-3'	This paper	N/A
qPCR murine *Dhcr24* primers: F:5'-CTCTGGGTGCGAGTGAAGG-3' R:5'-TTCCCCGGACCTGTTTCTGGAT-3'	This paper	N/A
qPCR murine *Ldlr* primers: F:5'-GAAGGCAGCTACAAGTGTGAG-3' R:5'-GGGGAGCAGACTGGTGTACT-3'	This paper	N/A
qPCR murine *Cxcl10* primers: F:5'-CCAAGTGCTGCCGTCATTTTC-3' R:5'-GGCTCGCAGGGATGATTTCAA-3'	This paper	N/A
qPCR murine *Il1b* primers: F:5'-AGCTTCCTTGTGCAAGTGTCT-3' R:5'-GACAGCCCCAGGTCAAAGGTT-3'	This paper	N/A
qPCR murine *Nos2* primers: F:5'-GTTCTCAGCCCAACAATACAAGA-3' R:5'-GTGGACGGGTCGATGTCAC-3'	This paper	N/A

REAGENT or RESOURCE	SOURCE	IDENTIFIER
qPCR murine *Retnla* primers: F:5'-CCAATCCAGCTAACTATCCCTCC-3' R:5'-ACCCAGTAGCAGTCATCCCA-3'	This paper	N/A
qPCR murine *Arg1* primers: F:5'-TTTTTCCAGCAGACCAGCTT-3' R:5'-AGAGATTATCGGAGCGGCCTT-3'	This paper	N/A
qPCR murine *Chil3* primers: F:5'-CAGGTCTGGCAATTCTTCTGAA-3' R:5'-GTCTTGCTCATGTGTGTAAGTGA-3'	This paper	N/A
qPCR murine *Mrc1* primers: F:5'-CTCTGTTCAGCTATTGGACGC-3' R:5'-CGGAATTTCTGGGATTCAGCTTC-3'	This paper	N/A
qPCR murine *Cd163* primers: F:5'-ATCCTCGGGGGTCATTCAGA-3' R:5'-GCCTGGGCTCTTGTTCCATT-3'	This paper	N/A
qPCR murine *Tgfb1* primers: F:5'-TTTTTCCAGCAGACCAGCTT-3' R:5'-AGAGATTATCGGAGCGGCCTT-3'	This paper	N/A
qPCR murine *Vegfa* primers: F:5'-CTGTGCAGGCTGCTGTAACG-3' R:5'-GTTCCCGAAACCCTGAGGAG-3'	This paper	N/A
ON-TARGETplus Non-targeting Pool	Dharmacon	Cat# D-001810–10-05
SMARTpool: ON-TARGETplus SREBF2 siRNA	Dharmacon	Cat# L-009549–00-0005
SMARTpool: ON-TARGETplus SREBF1 siRNA	Dharmacon	Cat# L-006891–00-0005
Recombinant DNA		
pcDNA3.1–2xFLAG-SREBP-2	Osborne lab: Toth et al., 2004	Addgene Plasmid #26807
Software and Algorithms		
Bowtie2 version 2.2.6	Langmead and Salzberg, 2012	http://www.bioinformatics.babraham.ac.uk/projects/fastqc
STAR Aligner	Dobin et al., 2013	https://github.com/alexdobin/STAR
HOMER version 4.7.2	Heinz et al., 2010	http://homer.ucsd.edu/homer
edgeR	Robinson et al., 2010	https://www.bioconductor.org/packages/release/bioc/html/edgeR.html
R	R core team, 2017	https://www.R-project.org/
Cuffdiff2	Trapnell et al., 2013	http://cole-trapnell-lab.github.io/cufflinks/cuffdiff/
GREAT version 3.0.0	McLean et al., 2010	http://bejerano.stanford.edu/great/public/html/
FlowJo v10	FlowJo, LLC	https://www.flowjo.com/
GraphPad Prism 6	GraphPad Software	https://www.graphpad.com/scientific-software/prism/

REAGENT or RESOURCE	SOURCE	IDENTIFIER
Ingenuity Pathway Analysis	Qiagen	www.qiagenbioinformatics.com/IPA
Seurat	Butler et al., 2018	https://satijalab.org/seurat/
Others		
Disposable biopsy punches, 4mm	Miltex	Cat# 33–34
Disposable biopsy punches, 8mm	Miltex	Cat# 33–37
Essential fatty acid deficient diet	Envigo	Cat# TD.84224
Essential fatty acid control diet	Envigo	Cat# TD.93184